

Observations of O I and Ca II Emission Lines in Quasars: Implications for the Site of Fe II Line Emission

Y. Matsuoka^{1,2}

S. Oyabu³

Y. Tsuzuki^{2,4}

and

K. Kawara¹

ABSTRACT

We present results of the near-infrared (IR) spectroscopy of six quasars whose redshifts range from 0.158 to 1.084. Combined with the satellite ultraviolet data, the relative line strengths of O I $\lambda 1304$, O I $\lambda 8446$, O I $\lambda 11287$, and the near-IR Ca II triplet are given. In addition, the corresponding O I line strengths measured in normal Seyfert 1s and narrow-line Seyfert 1s are collected from the literature. These lines are thought to emerge from the same gas as do the Fe II lines, so they are good tracers of the Fe II emission region within a broad emission line region (BELR) in active galactic nuclei (AGNs). In order to reveal the physical condition within the relevant emission region, we performed photoionized model calculations and compared them to the observations. It suggests that a rather dense gas with density $n_H \sim 10^{11.5} \text{ cm}^{-3}$ is present at an outer portion of the BELR, illuminated by the ionizing radiation corresponding to an ionization parameter $U \sim 10^{-2.5}$ and is primarily responsible for the observed O I, Ca II, and Fe II lines, based on the resemblance of their profiles. The three O I lines

¹Institute of Astronomy, The University of Tokyo, 2-21-1, Osawa, Mitaka, Tokyo 181-0015, Japan; matsuoka@ioa.s.u-tokyo.ac.jp.

²Visiting astronomer, United Kingdom Infrared Telescope which is operated by the Joint Astronomy Centre on behalf of the U.K. Particle Physics and Astronomy Research Council.

³Institute of Space and Astronautical Science, Japan Aerospace Exploration Agency, 3-1-1, Yoshinodai, Sagamihara, Kanagawa 229-8510, Japan.

⁴Institute for Cosmic Ray Research, The University of Tokyo, 5-1-5, Kashiwanoha, Kashiwa, Chiba, 277-8582, Japan.

are proven to be formed through Ly β fluorescence and collisional excitation. We also show that the $\lambda 1304$ bump typically observed in AGN spectra consists of the comparable contributions of O I and Si II multiplets, and we discuss the origin of such a strong Si II emission. The results are interpreted in the context of the locally optimally emitting cloud (LOC) scenario to find the plausible gas distribution within the BELR as a function of distance from the central source and density.

Subject headings: galaxies: active — galaxies: individual (3C 273, QSO B0850+440, 3C 232, QSO J1139–1350, PG 1148+549, PG 1718+481) — galaxies: quasars: emission lines — galaxies: Seyfert — line: formation

1. INTRODUCTION

The emission lines from singly ionized iron are one of the most prominent features in ultraviolet (UV) to optical spectra of many AGNs. They are considered to arise from the partly ionized gas present in a BELR. They dominate the heating and cooling of the emission region through a huge number of electronic transitions characteristic of the Fe $^{+}$ atom, which results in the Fe II “pseudocontinuum” observed in the AGN spectra.

It is important to understand the physics of the Fe II line formation for several reasons. First, since the Fe II lines carry a large amount of energy away from the BELR, it provides useful information about the energy budget of the emitting gas. Second, measurements of the Fe abundance in high-redshift quasars through their Fe II emission as a function of cosmic time could verify some cosmological parameters (Hamann & Ferland 1993; Yoshii et al. 1998). Many observations have been devoted to the Fe II flux measurements in high-redshift quasars for this purpose in recent years (e.g., Elston et al. 1994; Kawara et al. 1996; Dietrich et al. 2002, 2003; Iwamuro et al. 2002, 2004; Freudling et al. 2003; Maiolino et al. 2003). However, as has been pointed out by several authors (e.g., Verner et al. 2003; Baldwin et al. 2004; Tsuzuki et al. 2007), the Fe II line strengths could be strongly affected by some physical, nonabundance factors of the emitting gas, such as density and incident-ionizing radiation flux, so that a priori knowledge of them is definitely needed in order to deduce the Fe abundance.

There have been many studies of Fe II emission in AGNs. Netzer & Wills (1983) and Wills et al. (1985) modeled the Fe II emission of quasars using a model Fe $^{+}$ atom with energy levels up to ~ 10 eV and typical BELR parameters in order to compare them with observations. Their study was followed by, e.g., Sigut & Pradhan (1998, 2003) and Verner et al.

(1999, 2003), who made significant improvements both on the atomic data and on the physical processes included. Baldwin et al. (2004) calculated the Fe II and other emission-line strengths in a wide range of gas physical parameters and integrated them to reproduce the observed spectra in the context of the LOC (Baldwin et al. 1995) scenario. However, these studies using the observed shape and/or strength of the Fe II pseudocontinuum have several serious problems. From an observational viewpoint, it is extremely difficult to isolate the Fe II pseudocontinuum from the UV to optical spectrum of AGNs, which is usually made up of several continuum components besides emission lines, such as a power-law continuum and a Balmer continuum. Recently, Tsuzuki et al. (2006) presented quasar spectra with a wide wavelength coverage, extending from 1000 to 7300 Å, thus providing a detailed discussion on this issue. From a theoretical viewpoint, it is still not confirmed whether the included number of energy levels of the Fe^+ atom and excitation mechanisms are sufficient to reproduce the physical processes occurring in AGNs. Specifically, it is widely known that none of the current photoionized models can reproduce the observed strong optical Fe II emitters (e.g., Collin & Joly 2000) while the recent reverberation mapping results indicate a direct connection between the optical Fe II emission and the continuum radiation from the central source (Vestergaard & Peterson 2005).

Given the difficulties raised above, one approach to investigating the physical condition within the Fe II emission region is to use the lines emitted by simple atoms in the same region. Rodríguez-Ardila et al. (2002a) found that near-IR O I, Ca II, and Fe II lines have very similar profiles in the narrow-line Seyfert 1s (NLS1s), indicating that these low-ionization lines are arising from the same portion of the BELR. They also found a good correlation between the near-IR and optical Fe II emission, which implies a direct link between them in the sense that they are produced by the same excitation mechanisms. The correlation between O I and Ca II line widths and between Ca II and Fe II line strengths has also been reported for Seyfert 1s (Sy1s) and NLS1s (Persson 1988). Note that they are a natural consequence of similar ionization potentials of the relevant ions, i.e., 16.2 eV for Fe II, 13.6 eV for O I, and 11.9 eV for Ca II. Thus, O I and Ca II lines are good tracers of the interesting and important Fe II line-emission region in AGNs.

The first extensive study of the physical condition within an O I emission region in AGNs was presented by Grandi (1980). He found that O I $\lambda 8446$ lacks the narrow component that characterizes other permitted lines, leading to the conclusion that the line is purely a BELR phenomenon. Such a conclusion is also reported in Riffel et al. (2006). Grandi (1980) also suggested that O I $\lambda 8446$ is produced by Ly β fluorescence, which was later confirmed by the observation of I Zw 1, the prototype NLS1, by Rudy et al. (1989). Rodríguez-Ardila et al. (2002b) compiled the UV and near-IR O I line strengths of NLS1s (including I Zw 1) and of Sy1s, to investigate their flux ratios, and found that there must be an additional excitation

mechanism of O I λ 8446—besides Ly β fluorescence—which they concluded is collisional excitation. Matsuoka et al. (2005) found that the collisional processes are at work to a similar extent in quasars and suggested that the gas density in the relevant line emission region is not significantly different among NLS1s, Sy1s, and quasars. On the other hand, Ferland & Persson (1989) computed the strengths of various emission lines, including the UV and near-IR Ca II lines, and found that a very large column density ($\sim 10^{25}$ cm $^{-2}$) is needed in order to reproduce the observed relative strengths of these lines. However, previous studies have not yet revealed some important physical parameters of the emitting gas quantitatively, mainly due to the lack of sufficient data or precise modeling.

Here we present a new near-IR observation of six quasars with redshifts up to 1.084. Combined with the satellite UV data, the relative strengths of O I λ 1304, O I λ 8446, O I λ 11287, and the near-IR Ca II triplet (λ 8498, λ 8542, and λ 8662) are given. The purpose of the observation is twofold: to give a quantitative insight into the physical condition within the partly ionized region where O I, Ca II, and Fe II lines are emitted, by comparing the observations with precise model calculations; and to extend the observed O I and Ca II samples to higher redshifts than the previous measurements ($z < 0.18$) and to include quasars, which are important in the context of the Fe abundance investigation in high-redshift quasars. The observations are presented in §2, and compared model calculations are given in §3. A discussion of the results and their implications appear in §4. Finally our conclusions are summarized in §5.

2. OBSERVATIONS

2.1. Target Selection

Target quasars were selected from a UV spectral atlas of AGNs presented by Evans & Koratkar (2004). The strongest constraint on the target selection comes from their redshifts; O I λ 8446, O I λ 11287, and the near-IR Ca II triplet should fall within the atmospheric windows. It significantly reduced a number of possible targets, since these lines are too separated to be observed in the single near-IR band (J , H , or K). From the quasars satisfying this criterion, we selected those having the highest signal-to-noise ratios (S/Ns) around O I λ 1304 in the corresponding UV spectra, which constitute our final target list. The characteristics of the observed quasars are summarized in Table 1.

2.2. Near-Infrared Observation

A near-IR observation was carried out at the United Kingdom Infrared Telescope (UKIRT) using the UIST (UKIRT 1–5 μm Imager Spectrometer; Ramsay Howatt et al. 2004) on 2006 February 24. We adopted the standard UIST observing templates for faint point-source spectroscopy and for point-source imaging. An observational journal is given in Table 2 for the spectroscopy and in Table 3 for the imaging. The spectroscopic observation includes a flat, arc, and rationing star for each target, taken right before the target observation. The rationing stars were selected from the F4 – F9 type dwarf bright stars with moderately strong H I recombination lines and weak atomic lines, which are well suited for rationing low-resolution spectra. They were observed at air masses similar to the corresponding targets. The targets and the rationing stars were observed by nodding the telescope in such a way that they slid +6 $''$ and then –6 $''$ along the slit. A 0.6 $''$ slit yielded an instrumental resolution of \sim 750 km s^{-1} , while the pixel scale is 0.12 $''$. The imaging observation consists of dark, flat, and standard stars taken right before the target observation, while the self-flats were used for some faint sources. The standard stars were taken from the UKIRT Faint Standards (Hawarden et al. 2001; Legett et al. 2006) so that they could be observed at air masses similar to the targets. The targets and the standard stars were observed at five positions on the detector, offset by 20 $''$ for the targets and by 10 $''$ for the standard stars. The sky condition was photometric throughout the night, and the average seeing was 0.6 $''$.

We used the standard method to reduce the data, including removal of dark, flat-fielding, and sky subtraction using the reduction software IRAF.¹ Wavelength calibration was achieved using argon arc-lamp spectra. In order to calibrate the sensitivity variation along the dispersion axis, the rationing-star spectra—from which the intrinsic H I recombination absorption lines had been removed—were compared with the blackbody spectra with corresponding temperatures, i.e., 6500 K for F4 V type stars, 6250 K for F7 V, and 6000 K for F8 V and F9 V. Finally, photometric calibration was obtained by using the imaging data. Measured *J*- or *H*-band magnitudes of the quasars are listed in the last two columns of Table 1. Statistical errors of the photometry were less than 0.01 mag for all targets.

We show the reduced spectra along with the sensitivity curves in Figures 1 – 2. The redshifts measured in the near-IR spectra were in good agreement with those measured in the UV spectra (Evans & Koratkar 2004).

¹IRAF is distributed by the National Optical Astronomy Observatory, which is operated by the Association of Universities for Research in Astronomy, Inc., under cooperative agreement with the National Science Foundation.

2.3. Ultraviolet Data

Ultraviolet spectra of the quasars were obtained from 1991 January to 1993 July using the Faint Object Spectrograph (FOS) onboard the *Hubble Space Telescope*² (*HST*). In the current work, we used those reduced by Evans & Koratkar (2004). They extensively recalibrated all pre-COSTAR (Corrective Optics Space Telescope Axial Replacement) archival FOS UV and optical spectrophotometry of AGNs with the latest algorithms and calibration data. If multiple observations of the same source were available, they were combined after being scaled to each other in such a way that the resultant spectrum would have the highest possible S/N. The UV spectra around O I λ 1304 used in this work are shown in Figure 3.

2.4. Emission-Line Measurements

Emission lines in the UV and the near-IR spectra were manually identified, and their intensities were measured by summing up all the flux above the local continuum, which was placed by the interpolation method using the observed fluxes in the continuum windows at both sides of the lines. The continuum windows were carefully selected to not be contaminated by weak emission lines based on the high-S/N spectra of NLS1s presented by Laor et al. (1997b) and Rodríguez-Ardila et al. (2002a). A Voigt profile was fitted to continuum-subtracted spectra by the least χ^2 method to measure line widths for some lines (see below). As described by Glikman et al. (2006), a single-component Voigt profile is a better choice than a multi-component Gaussian profile when fitting lines with a low S/N. This is the case for some of the measured lines in our spectra. When several lines were blended, we fitted a multi-component Voigt profile to the continuum-subtracted spectra in order to deblend the feature. Then the total flux was divided into each component, according to the fitted profiles.

Although the λ 1304 bump results from a blending of an O I triplet at λ 1302, λ 1305, and λ 1306, and a Si II doublet at λ 1304 and λ 1309, deblending of these components is hopeless, considering the broad line widths of quasars. Thus, we regarded this feature as a single component in the flux-measurement procedure. Its constitution is closely discussed in §4.2. On the other hand, when fitting blended O I λ 8446 and the Ca II triplet (λ 8498, λ 8542, and λ 8662), we fixed their relative wavelength centroids and relative intensities of the Ca II triplet to the values found in I Zw 1 (Rudy et al. 2000) in order to avoid too many

² This publication is based on observations made with the NASA/ESA Hubble Space Telescope, obtained from the data archive at the Space Telescope Science Institute, which is operated by the Association of Universities for Research in Astronomy, Inc., under NASA contract NAS 5-26555.

parameters being used in the fitting. This procedure was proven to work very well, since the blueward part of O I $\lambda 8446$ is almost free from contamination of the Ca II components. In some objects, there is an unidentified weak emission line at the blueward part of the blend feature, or the redward part falls in the atmospheric absorption bands, which limits the available wavelength range used in the fitting and flux measurements. In these cases, the correction was applied to the flux falling in outside the flux-measured wavelength range according to the fitted Voigt profiles. The fits for the relevant O I and Ca II lines in 3C 273 are shown in Figure 4.

The measured line fluxes are summarized in Table 4. The quoted errors were estimated by the $\Delta\chi^2$ test, which reflect the uncertainties in determining the underlying continuum level (i.e., the S/N in the continuum windows) and in deblending the blended feature.

2.5. Variability and Reddening Effects

It is widely known that quasars are highly variable. Since the dates of the UV observations are separated from that of the near-IR observation by more than 15 yr, a possible variability effect should be carefully examined before comparing the UV and the near-IR spectra. In fact, the observed quasars show brightness variations in the J or H band by as large as 0.6 mag from the dates of the Two Micron All Sky Survey³ (2MASS) observations as shown in Table 1. However, amounts of the emission-line variabilities corresponding to these continuum variations are rather uncertain. Monitoring observations of the well-known variable Seyfert NGC 5548 revealed that when the UV continuum varied its brightness by about 300%, the flux variation in Mg II, one of the low-ionization lines such as O I and Ca II, was only about 10% (Dietrich & Kollatschny 1995). On the other hand, Vestergaard & Peterson (2005) showed that the variability amplitude of optical Fe II emission is 50–75% of that of $H\beta$, whose variation is comparable to those in the continuum, and UV Fe II emission varies with an even larger amplitude. The response of the individual lines to the continuum variation depends on their formation processes and gas distribution within the BELR (e.g., O’Brien et al. 1995), whose quantitative estimates are far beyond the scope of this paper. We give notes as to how the possible variability could affect our conclusions in the following sections, when needed.

Another source of errors in comparing the UV and the near-IR spectra is the extinc-

³ This publication makes use of data products from 2MASS, which is a joint project of the University of Massachusetts and the Infrared Processing and Analysis Center/California Institute of Technology, funded by the National Aeronautics and Space Administration and the National Science Foundation.

tion by dust both in the Galaxy and in the quasar host galaxies. We adopted the Galactic extinction values presented by Schlegel et al. (1998), which are derived from the far-IR observations in two satellite missions, the *Infrared Astronomical Satellite (IRAS)* and the *Cosmic Background Explorer (COBE)*. Their extinction map has a relatively fine resolution of $6.1'$ and an accuracy of 16%. Corresponding dereddening of the spectra was achieved by using the Galactic extinction curve presented by Pei (1992).

On the other hand, much less has been confirmed about the internal reddening of quasars. Cheng et al. (1991) found that UV continuum slopes for a wide variety of AGNs were essentially the same to within their measuring errors, corresponding to a reddening amount of $E_{B-V} \lesssim 0.1$ mag. In the optical, De Zotti & Gaskell (1985) showed that both the broad emission lines and continua of radio-quiet Seyfert galaxies typically have a reddening of $E_{B-V} = 0.25$ mag. Assuming the Small Magellanic Cloud (SMC) extinction curve (Hopkins et al. 2004) presented by Pei (1992), this translates to $E_{1304-8446}$, the color excess between 1304 and 8446 Å, of 3.58 mag. Hence, the measured UV to near-IR line ratios should be regarded as the lower limits on their intrinsic values, which could be an order of magnitude or more larger than observed. As in the case of the variability, the possible changes in our conclusions due to the internal reddening effect are noted in the following sections.

3. COMPARISON WITH MODELS

In this section, we aim to investigate the physical condition within the O I and Ca II emission region by comparing the observed line strengths with model predictions. It is becoming a common understanding that the BELR is composed of gas with widely distributed physical parameters and that each emission line arises from its preferable environment (Baldwin et al. 1995). In order to reveal the distribution functions of gas in such a complex system, it is crucial to constrain which region in the parameter space actually dominates observed emission of the specific lines.

3.1. Observational Constraints

The observed equivalent widths (EWs) of O I $\lambda 8446$ and photon flux ratios of O I $\lambda 11287$ and the near-IR Ca II triplet to O I $\lambda 8446$ are used to constrain the models. Hereafter, they are expressed as EW (O I $\lambda 8446$), O I $n(\lambda 11287)/n(\lambda 8446)$, and $n(\text{Ca II})/n(\text{O I } \lambda 8446)$, respectively. These emission lines have been revealed to arise from the same portion of the

BELR among the various lines observed (see §1), which significantly simplifies the interpretation of the observed quantities. They are summarized in Table 5 (see the quasar section) for the quasars observed in this work and for the quasar PG 1116+215 ($z = 0.176$) studied by Matsuoka et al. (2005). A representative wavelength of 8579 Å was used to convert total flux of the Ca II triplet to the photon number flux.

The observed values of O I $n(\lambda 11287)/n(\lambda 8446)$ are fairly similar from quasar to quasar except for 3C 232. The mean value is 0.46 ± 0.18 , where the quoted error reflects a scatter among the quasars. It should be an excellent indicator of the emitting gas physics, since several important but uncertain parameters could be nearly canceled out, which include chemical composition and the covering fraction of the line-emitting gas seen from the central continuum source. The reddening effect on the ratio would also be small. That observed in 3C 232 is significantly different from other quasars, which is apparently due to the extreme weakness of O I $\lambda 8446$. It is noted that Ca II is also very weak in 3C 232. Since there are no distinct features in the sensitivity curve around the relevant wavelength range, the weakness is not a consequence of the instrumental or the atmospheric absorption effects. On the other hand, no appropriate models considered below could reproduce such a large value of the O I $n(\lambda 11287)/n(\lambda 8446)$ ratio. Hence, we concluded that some unusual effects concealed a large fraction of emission lines around 8500 Å and decided to exclude this quasar from the sample to be compared with model calculations below.

EW (O I $\lambda 8446$) represents the efficiency of reprocessing the incident continuum radiation into the line emission. It also depends on the gas covering factor and abundance of the relevant element (oxygen in this case). Models should reproduce the observed values, $\text{EW}(\text{O I } \lambda 8446) > 10 \text{ \AA}$, with reasonable values of these parameters.

The Ca II triplet is observed to have a strength comparable to O I $\lambda 8446$. The ratio between them, predicted in model calculations, also depends on the assumed chemical composition (Ca/O in this case) of the emitting gas. Hamann & Ferland (1999) showed that the Mg/O abundance ratio varies from the solar value within a factor of 2 through the course of galaxy evolution in either the solar neighborhood or the giant elliptical model. Since Ca and Mg belong to the α -elements so that their production rates should not significantly differ from each other, the Ca/O ratio could also deviate from the solar value by a similar amount.

3.2. Model Calculations

A partial Grotrian diagram of an O I atom is given in Figure 5. In the simplest case, O I $\lambda 11287$, $\lambda 8446$, and $\lambda 1304$ are formed through Bowen resonance-fluorescence by Ly β , or Ly β

fluorescence; Ly β photons pump up the ground-term ($2p\ ^3P$) electrons to the excited $3d\ ^3D^0$ level, from which they cascade down to the ground term through $3p\ ^3P$ and $3s\ ^3S^0$, producing the $\lambda 11287$, $\lambda 8446$, and $\lambda 1304$ line photons. Note that the pumped $2p\ ^3P - 3d\ ^3D^0$ transition energy corresponds to 1025.77 \AA so that it falls within a Doppler core of Ly β (1025.72 \AA) for gas at a temperature of 10^4 K . As a result, the photon flux ratios between these lines should be unity. However, there could be other excitation mechanisms that alter the ratios, which are collisional excitation, continuum fluorescence, and recombination. Kwan & Krolik (1981) reported that trapping of $\lambda 1304$ becomes important in sustaining the population at $3s\ ^3S^0$ level with the large column density typical of the BELR cloud, leading to collisional excitation of the $\lambda 8446$ emission. If $\lambda 8446$ also became optically thick, an additional $\lambda 11287$ excitation would follow. Continuum fluorescence of the ground-term ($2p\ ^3P$) electrons could also produce these lines, as well as other lines, such as $\lambda 13165$ (see Fig. 5). This mechanism is known to be an important contributor to the $\lambda 8446$ emission observed in some Galactic objects (Grandi 1975a,b; Rudy et al. 1991). While recombination is another source of the O I line emissions, its contribution is known to be negligible in the BELR gas (Grandi 1980; Rodríguez-Ardila et al. 2002b).

We performed model calculations in the framework of the photoionized BELR gas using the photoionization code Cloudy, version 06.02 (Ferland et al. 1998). The chosen form of the incident continuum shape is a combination of a $f_\nu \propto \nu^{\alpha_{\text{uv}}} \exp(-h\nu/kT_{\text{cut}})$ UV bump with an X-ray power law of the form $f_\nu \propto \nu^{\alpha_x}$ spanning 13.6 eV to 100 keV . The UV bump is also cut off in the infrared with a temperature $kT_{\text{IR}} = 0.01\text{ Ryd}$, corresponding to $9.1\text{ }\mu\text{m}$. The UV and X-ray continuum components are combined using a UV to X-ray logarithmic spectral slope α_{ox} , which is defined by $f_\nu(2\text{ kev})/f_\nu(2500\text{ \AA}) = 403.3^{\alpha_{\text{ox}}}$. We adopted a parameter set of $[T_{\text{cut}}, \alpha_{\text{uv}}, \alpha_x, \alpha_{\text{ox}} = (1.5 \times 10^5)\text{ K}, -0.2, -1.8, -1.4]$. It is essentially the same as those of Tsuzuki et al. (2006, 2007) who derived these parameter values by combining the results of the thermal accretion disk models (Krolik & Kallman 1988; Binette et al. 1989; Zheng et al. 1995) and the observed spectrum of the quasar PG 1626+554 which has typical spectral properties among their 14 quasar samples.

The BELR gas was modeled to have a constant hydrogen density n_{H} (cm^{-3}) and exposed to the ionizing continuum radiation with a photon flux of Φ ($\text{s}^{-1}\text{ cm}^{-2}$). The incident-ionizing continuum flux is expressed with an ionization parameter in the calculation $U \equiv \Phi/(n_{\text{H}} c)$, where c is the speed of light, since predicted line strengths tend to be similar along the same values of U . We performed the calculations with the (n_{H}, U) sets in a range of $10^{7.0}\text{ cm}^{-3} \leq n_{\text{H}} \leq 10^{14.0}\text{ cm}^{-3}$ and $10^{-5.0} \leq U \leq 10^{0.0}$ stepped by 0.5 dex, which should more than cover the parameter space of the BELR gas. We began with a BELR gas with $N_{\text{H}} = 10^{23}\text{ cm}^{-2}$ and $v_{\text{turb}} = 0\text{ km s}^{-1}$, where N_{H} is the gas column density and v_{turb} the microturbulent velocity. Chemical composition was assumed to be solar. We hereafter refer to this model

as the standard model, or model 1; input parameters are summarized in Table 6.

In the calculations, the O I atom was treated as a 6 electron energy-level system including $3s\ ^3S^0$, $4s\ ^3S^0$, $2p\ ^3P$, $3p\ ^3P$, $4p\ ^3P$, and $3d\ ^3D^0$ levels (see Fig. 5; Ferland 2004). Note that the contribution from recombination is not included in the predicted line strengths, since the effective recombination coefficients for the O I lines are not known for densities as large as those in the BELR (G. J. Ferland 2006, private communication). However, it is expected to be negligible compared to other excitation mechanisms as reported by Grandi (1980) and Rodríguez-Ardila et al. (2002b). They showed that the observed strengths of O I $\lambda 7774$, the quintet counterpart to O I $\lambda 8446$, were less than 10% of those of $\lambda 8446$ (see Table 8), while the ratio between them should be $\lambda 7774/\lambda 8446 \sim 1.7$ in the pure recombination case based solely on the relative statistical weights (Grandi 1980). On the other hand, we found that the ratio should be $\lambda 7774/\lambda 8446 \sim 7.2$ in the pure recombination case using the effective recombination coefficients in the low-density limit (appropriate for the normal Galactic gaseous nebulae) presented by Péquignot et al. (1991). Even if we assumed that the observed $\lambda 7774$ was exclusively produced by recombination, its contribution to the $\lambda 8446$ is less than a few percent.

3.3. Results

3.3.1. The Standard Model

We show the calculated O I photon flux ratios $n(\lambda 11287)/n(\lambda 8446)$ and $n(\lambda 1304)/n(\lambda 8446)$ in Figure 6 as a function of the gas density n_H and the ionization parameter U . Note that the incident-ionizing continuum flux Φ increases toward the direction shown by the arrows in the figure. Both ratios are almost unity at the canonical BELR parameters $(n_H, U) = (10^{10} \text{ cm}^{-3}, 10^{-2})$, which refer to the region where high-ionization lines (such as C IV) are emitted (Davidson & Netzer 1979), indicating that Ly β fluorescence is actually the main formation mechanism of these O I lines. As the density becomes large relative to the canonical parameter, both ratios decrease due to the collisional enhancement of the $\lambda 8446$ photons. On the other hand, continuum fluorescence becomes important as incident continuum flux is significantly decreased, due to a significant suppression in Ly β formation. It results in $\lambda 1304$ photons not accompanied by those of $\lambda 8446$, as well as $\lambda 8446$ not accompanied by $\lambda 11287$, so that $n(\lambda 11287) < n(\lambda 8446) < n(\lambda 1304)$. The results of our observation, O I $n(\lambda 11287)/n(\lambda 8446) = 0.46 \pm 0.18$, clearly indicate that Ly β fluorescence is not the only excitation mechanism of these lines. The excess $\lambda 8446$ photons relative to $\lambda 11287$ should be produced through either collisional excitation or continuum fluorescence, depending on the physical condition within the emitting gas.

The two excitation mechanisms can be distinguished by their continuum reprocessing efficiency, which converts the incident continuum radiation into the relevant line emission, through the observed EW (O I $\lambda 8446$). We plot the calculated values of them in Figure 7 (*top right*), assuming a covering factor of 1.0, as well as the O I $n(\lambda 11287)/n(\lambda 8446)$ ratios for reference (*top left*). Since the covering factor in actual quasars may be much smaller, all the parameter sets satisfying $\text{EW}(\text{O I } \lambda 8446) > 10 \text{ \AA}$ are consistent with the observation. However, it is noted that the covering factor should not be much less than 0.1; in such a situation, the predicted EW (O I $\lambda 8446$) falls well below those observed on the whole parameter plane. It is also true in other models described below. Figure 7 shows that the low density gas in which continuum fluorescence dominates the O I line formation predicts O I $\lambda 8446$ at the level of $\text{EW}(\text{O I } \lambda 8446) < 1 \text{ \AA}$, which can hardly reproduce the observation. On the other hand, there is a large area consistent with both the observed O I $n(\lambda 11287)/n(\lambda 8446)$ ratios and EW (O I $\lambda 8446$) at the high-density side where collisional excitation is at work. Thus, we concluded that the observed O I lines are produced by a combination of Ly β fluorescence and collisional excitation.

We show the calculated $n(\text{Ca II})/n(\text{O I } \lambda 8446)$ ratios in Figure 7 (*bottom left*) to further constrain the model parameters. The fact that these two emissions are observed to have comparable strengths, combined with the results from the O I line strengths, finely restricts the gas density to be around $n_{\text{H}} = 10^{11.5} \text{ cm}^{-3}$. However, the model predictions could vary within a factor of 2, depending on the assumed chemical composition as described in §3.1. It also depends on the assumed column density N_{H} and increases by up to a factor of 3 when it is changed from $N_{\text{H}} = 10^{23}$ to 10^{25} cm^{-2} , as shown in Figure 8. Thus, we required that the predicted Ca II/O I $\lambda 8446$ ratio should fall in the range $0.1 < n(\text{Ca II}) / n(\text{O I } \lambda 8446) < 5.0$. This constraint still effectively excludes the high-density ($n_{\text{H}} > 10^{12.0} \text{ cm}^{-3}$) and low ionization parameter ($U < 10^{-2.5}$) models in which the Ca II emission is significantly overpredicted.

The top left, top right, and bottom left panels of Figure 7 are shown in a single plot in the bottom right panel of the same figure. The constraints from the observed values of O I $n(\lambda 11287)/n(\lambda 8446)$, EW (O I $\lambda 8446$), and $n(\text{Ca II})/n(\text{O I } \lambda 8446)$ are shown by thick solid lines, thin solid lines, and the shaded area, respectively. The models consistent with all the constraints are marked with diamonds, which are $n_{\text{H}} = 10^{11.5} \text{ cm}^{-3}$, and $U = 10^{-2.5}$ and $10^{-3.0}$. However, since the covering factors in actual quasars are known to be ~ 0.1 , we favor the models predicting $\text{EW}(\text{O I } \lambda 8446) > 100 \text{ \AA}$ despite the formal constraint of $> 10 \text{ \AA}$. Thus, we concluded that the best-fit parameter set to the observations is $(n_{\text{H}}, U) = (10^{11.5} \text{ cm}^{-3}, 10^{-3.0})$ in the standard model. The predicted line strengths in this specific model are summarized in Table 7.

Next we investigated the line strengths as a function of gas column density in the range $N_{\text{H}} = 10^{17} - 10^{25} \text{ cm}^{-2}$. A calculation was performed for the gas with $N_{\text{H}} = 10^{25} \text{ cm}^{-2}$, while other input parameters are identical to the standard model with $(n_{\text{H}}, U) = (10^{11.5} \text{ cm}^{-3}, 10^{-3.0})$, and the cumulative ratios of O I $n(\lambda 11287)/n(\lambda 8446)$, O I $n(\lambda 1304)/n(\lambda 8446)$, and $n(\text{Ca II})/n(\text{O I } \lambda 8446)$, as well as the cumulative flux of O I $\lambda 8446$, are plotted against the column density measured from the illuminated surface in Figure 8. The O I $\lambda 8446$ emission is mainly built up before the column density $N_{\text{H}} = 10^{23} \text{ cm}^{-2}$ is reached, and the deeper region contributes only $\sim 10\%$ to the emergent emission. Correspondingly, the two O I flux ratios stay nearly constant between $N_{\text{H}} = 10^{22}$ and 10^{25} cm^{-2} . On the other hand, the $n(\text{Ca II})/n(\text{O I } \lambda 8446)$ ratio becomes ~ 2 times larger when the column density is increased from $N_{\text{H}} = 10^{23}$ to 10^{25} cm^{-2} . This effect was first pointed out by Ferland & Persson (1989) and is already taken into account in the above arguments. Hence, we concluded that the assumed column density does not significantly change the results from the standard model unless it is much smaller than $\sim 10^{22} \text{ cm}^{-2}$. Note that the O I line formation would be significantly suppressed in such a thin gas (see Fig. 8) so that the EWs fall well below the observed values.

3.3.2. Other Models: Microturbulence and Incident Continuum

Some BELR models indicate a presence of the microturbulence within the gas, which includes a large velocity gradient in a wind (e.g., Königl & Kartje 1994) and nondissipative magnetohydrodynamic waves in magnetically confined clouds (Rees 1987; Bottorff & Ferland 2000). We performed another set of calculations with the microturbulence included, whose velocity is v_{turb} . It is known to have a large influence on the Fe II line strengths through a combined effect of the increased continuum fluorescence rate and the decreased line optical depth (Netzer & Wills 1983; Verner et al. 1999). Using a strong dependency, Verner et al. (2003) showed that $v_{\text{turb}} = 5 - 10 \text{ km s}^{-1}$ gives the most plausible values to account for the observed Fe II and Mg II emissions. On the other hand, Baldwin et al. (2004) reported that the photoionized BELR models cannot reproduce both the observed shape and EW of the Fe II UV bump unless the considerable amount of microturbulent velocity corresponding to $v_{\text{turb}} \geq 100 \text{ km s}^{-1}$ is included. Thus, we considered two models with the microturbulent velocity set to $v_{\text{turb}} = 10 \text{ km s}^{-1}$ (model 2) and 100 km s^{-1} (model 3). The input parameters of these models are summarized in Table 6.

The results in models 2 and 3 are rather similar to the standard model (Fig. 7), while the whole patterns of contour are shifted a little toward a high-density regime as the microturbulent velocity is increased. It is thought to be due to the decreased optical depth in O I

$\lambda 1304$, which then reduces the electron population in the $3s\ 3S^0$ level and thus the collisional excitation rate of O I $\lambda 8446$. As a result, it has to be compensated by the increased particle density to reproduce the observed degree of collision rate. It is also noted that the predicted EWs of O I lines are moderately decreased on the whole (n_{H}, U) parameter plane in model 3. Since the difference in the wavelengths of Ly β (1025.72 Å) and the pumped O I transition $2p\ 3P - 3d\ 3D^0$ (1025.77 Å) corresponds to the velocity of 15 km s $^{-1}$, the Ly β fluorescence efficiency is reduced in such a turbulent gas. The best-fit (n_{H}, U) parameters are determined in the same manner as in the standard model and listed in Table 7, which are $(n_{\text{H}}, U) = (10^{11.5} \text{ cm}^{-3}, 10^{-2.5})$ in model 2 and $(10^{12.0} \text{ cm}^{-3}, 10^{-2.5})$ in model 3. The predicted line strengths in these specific models are also listed in the table.

Finally, we changed the incident continuum shape to be much harder as suggested by Korista et al. (1997), which has the form $(T_{\text{cut}}, \alpha_{\text{uv}}, \alpha_{\text{x}}, \alpha_{\text{ox}}) = (10^6 \text{ K}, -0.5, -1.0, -1.4)$. It was also adopted by Baldwin et al. (2004). The microturbulent velocity is set to $v_{\text{turb}} = 100 \text{ km s}^{-1}$, which makes this model identical to model 8 of Baldwin et al. (2004). Model 8 was considered to reproduce both the observed shape and EW of the Fe II UV bump observed in AGNs with strong Fe II emission, and was proven to be one of the successful models (see §4.4 for more discussions). This is our model 4, whose input parameters are summarized in Table 6. Although the incident continuum shape is dramatically changed, the results are nearly identical to those in model 3, except that the predicted O I EWs are further decreased. The best-fit parameters are identical to model 3, $(n_{\text{H}}, U) = (10^{12.0} \text{ cm}^{-3}, 10^{-2.5})$. They are listed in Table 7 along with the predicted line strengths.

4. DISCUSSION

4.1. Excitation Mechanisms of the O I Lines

Our results indicate that the O I emission observed in quasars is formed through Ly β fluorescence and collisional excitation in gas with a density of $n_{\text{H}} \sim 10^{11.5} \text{ cm}^{-3}$, illuminated by the ionizing radiation corresponding to the ionization parameter $U \sim 10^{-2.5}$. It can be tested by investigating the observed strengths of other O I lines, which should or should not be accompanied by the strongest three lines, $\lambda 1304$, $\lambda 8446$, and $\lambda 11287$, in each excitation mechanism. We list the observed flux ratios of these lines measured to date in Table 8. Theoretical predictions of the ratios for the four possible excitation mechanisms, i.e., Ly β fluorescence, collisional excitation, continuum fluorescence, and recombination, are collected from the literature and also listed. In the case of pure Ly β fluorescence, all the ratios listed in the table should be zero; actually, this is satisfied in most objects with one exception, 1H 1934–063. The Ly β fluorescence plus collisional excitation from the $3s\ 3S^0$ level, which

our results indicate, would also predict all the ratios in the table to be nearly zero because the collisional excitation would predominantly produce the $\lambda 8446$ line photons against other lines listed.

The detection of $\lambda 7774$ in 1H 1934–063 led Rodríguez-Ardila et al. (2002b) to conclude that collisional excitation plays an important role in the O I line formation in NLS1s. They stated that the observed $\lambda 7774/\lambda 8446$ ratio is ~ 0.2 after the removal of Ly β fluorescence contribution, which is consistent with the theoretical prediction of pure collisional excitation given by Grandi (1980) ($\lambda 7774/\lambda 8446 \sim 0.3$; the “collisional excitation” row in Table 8). However, the prediction was derived from the collisional cross sections only from the ground term ($2p\ ^3P$). It should be an oversimplification because the collisional excitation from the excited $3s\ ^3S^0$ level, which we have shown is a large contributor to the $\lambda 8446$ emission, is not included. Then the observed strength of $\lambda 7774$ in 1H 1934–063, as large as 20% of $\lambda 8446$ (after Ly β fluorescence contribution was subtracted), should be attributed to other excitation mechanisms. Since another line, $\lambda 7990$, is also detected in similar strength in 1H 1934–063, recombination might be working to some extent and producing these emissions, as Rodríguez-Ardila et al. (2002b) recognized. An absence of the fourth mechanism, continuum fluorescence, is evident from the observed weakness of $\lambda 13165$; it is detected in none of the observed samples, while it should have a strength comparable to $\lambda 11287$ in the pure continuum fluorescence case (Grandi 1980).

Yet another mechanism of the O I line formation was suggested by Grandi (1983), in which the $3s\ ^3S^0$ level could decay to the metastable terms of the ground configuration via the semiforbidden lines $\lambda 1641$ and $\lambda 2324$ (see Fig. 5). He suggested that fully half of the $\lambda 1304$ photons would be destroyed by this mechanism in the typical BELR cloud. However, Laor et al. (1997b) reported that they found no strong line at 1641 \AA in the spectrum of I Zw 1 and that such a line cannot add more than $\sim 30\%$ to the observed $\lambda 1304$ flux.

4.2. Constitution of the $\lambda 1304$ Bump

The $\lambda 1304$ bump typically seen in AGN spectra is the result from a blending of an O I triplet at $\lambda 1302.17$, $\lambda 1304.86$, and $\lambda 1306.03$, with a mean laboratory wavelength of 1303.50 \AA (Verner et al. 1996; Constantin et al. 2002) and a Si II doublet at $\lambda 1304.37$ and $\lambda 1309.27$ (mean laboratory wavelength 1307.63 \AA , hereafter referred to as the $\lambda 1308$ doublet). This blending is very strong in most quasars, preventing a reliable estimate of relative contributions of O I and Si II to the blend. Accordingly, deblending of the bump has been tried mostly for NLS1s and quasars having relatively narrow broad emission line profiles. Baldwin et al. (1996) performed the method to fit the synthetic spectra constructed separately for each

quasar to deblend the bump. Although they could not firmly determine the strengths of both the O I and Si II components for any single quasar, the fitting results show that the O I fractions in the bump vary in the range from <30% to >60%. More plausible measurements were achieved for I Zw 1 by Laor et al. (1997b). The Si II $\lambda 1309.27$ component is clearly detected in I Zw 1, which enables the reliable estimate of the O I and Si II fractions in the blend. Their template fit shows that 50% (56%) of the bump flux is due to O I in the optically thick (thin) Si II doublet case. Rodríguez-Ardila et al. (2002b) applied the same method to three NLS1s and found that the average portion of the O I flux is 75%.

Now we investigate the composition of the $\lambda 1304$ bump from the standpoint of the photoionized model calculations. We are particularly interested in whether the dominant contributor to the bump, i.e., either O I or Si II, actually varies from quasar to quasar as shown by Baldwin et al. (1996). We plot the O I $n(\lambda 1304)/n(\lambda 8446)$ versus $n(\lambda 11287)/n(\lambda 8446)$ relation in Figure 9, which is calculated in models 1 – 4 with the (n_{H}, U) parameters around the best-fit values with which the O I line formation is dominated by Ly β fluorescence and collisional excitation, as revealed above. The range of the observed $n(\lambda 11287)/n(\lambda 8446)$ value is shown by two dotted lines. In order to obtain a rough estimate independent of the selected model, we regard the predicted $n(\lambda 1304)/n(\lambda 8446)$ values enclosed by two dashed lines in the figure, drawn to include most of the points in the observed $n(\lambda 11287)/n(\lambda 8446)$ range, as the allowed values against $n(\lambda 11287)/n(\lambda 8446)$. These lines are expressed as

$$n(\lambda 1304)/n(\lambda 8446) = 1.15 \times n(\lambda 11287)/n(\lambda 8446) - (0.20 \pm 0.05). \quad (1)$$

Then the observed $n(\lambda 11287)/n(\lambda 8446)$ ratios and the bump (O I + Si II $\lambda 1304$) flux give the estimates of the O I fraction in the bump; the results are listed in Table 9. It shows that the O I fractions actually vary from quasar to quasar by a significant amount, ranging from $\lesssim 20\%$ in QSO J1139–1350 to $\gtrsim 60\%$ in 3C 273 and QSO B0850+440. While it was hoped that O I $\lambda 1304/\lambda 8446$ ratio would be a reliable reddening indicator of AGNs as long as its intrinsic value was accurately determined (e.g., Rodríguez-Ardila et al. 2002b), our results show that it is more difficult than had been expected without accurate line deblending or precise model calculations.

The derived fluxes of the Si II $\lambda 1308$ doublet are comparable or even a few times larger than those of O I $\lambda 1304$. However, it cannot be reproduced in our model calculations; the equivalent width of Si II $\lambda 1308$ is at most 3 Å on the whole (n_{H}, U) parameter plane in all models while $\text{EW} (\text{O I } \lambda 1304) \sim 100$ Å (10 Å if the covering factor is set to 0.1) with the best-fit parameters. Changing the assumed column density does not settle the problem, in which the Si II $\lambda 1308$ flux is enhanced only by $\sim 20\%$ when N_{H} is increased from 10^{23} to 10^{25} cm $^{-2}$. A possible explanation comes from the LOC scenario. We plot the distribution of $\text{EW} (\text{Si II } \lambda 1308)$ as a function of the gas density n_{H} and the ionization parameter U

in the standard model in Figure 10, which shows that the Si II $\lambda 1308$ emission arises from the vast area on the parameter plane in similar strengths, while O I emission arises from the relatively limited region (Fig. 7, *top right*). Thus, the LOC-type integration over the parameter plane could significantly strengthen the predicted Si II emission relative to O I, which could account for the observations. An alternative way to interpret the strong Si II $\lambda 1308$ emission is an unusually large microturbulent velocity present in the emitting gas, as suggested by Bottorff et al. (2000). According to their calculations, Si II $\lambda 1308$ is one of the most enhanced lines by the increased microturbulent velocity. They showed that very large values of the microturbulent velocity are required in order to reproduce the Si II line strengths reported by Baldwin et al. (1996), which correspond to $v_{\text{turb}} > 1000 \text{ km s}^{-1}$. Si II $\lambda 1308$ is enhanced by more than 2 orders of magnitude in such a highly turbulent gas compared to the no microturbulence case, while O I $\lambda 1304$ is reduced by more than 80% due to the significant suppression in the Ly β fluorescence rate.

Still other mechanisms of the Si II $\lambda 1308$ enhancement are discussed in detail in Baldwin et al. (1996, Appendix C). They suggested that dielectric recombination or charge transfer might produce significant emission in the highly excited Si II lines, including $\lambda 1308$, in order to account for their observed strengths relative to the lowest line, $\lambda 1814$, in one of the gas components (dubbed “component A”) in the quasar Q0207–398. Note that component A was found to have an extremely high ($n_{\text{H}} \gtrsim 10^{12.5} \text{ cm}^{-3}$) gas density, which they stated makes the above processes competitive through the thermalization of all resonance lines.

Finally, it should be noted that the intrinsic values of O I + Si II $\lambda 1304$ /O I $\lambda 8446$ ratio could be larger than measured by more than an order of magnitude due to the internal reddening effect. Then the O I fractions in the $\lambda 1304$ bump would become even smaller than derived here, corresponding to the applied amounts of dereddening. An additional but probably smaller uncertainty comes from the possible variability event of the emission lines (see §2.5).

4.3. Situation in Other Type 1 AGNs

Observations of the O I flux ratio between $\lambda 8446$ and $\lambda 11287$ in Sy1s and NLS1s have been reported to date (Laor et al. 1997b; Rudy et al. 2000; Rodríguez-Ardila et al. 2002b), which are listed in Table 5 (see the Sy1 and NLS1 sections). The ratio of 0.55 ± 0.08 in the Sy1 is very similar to those of quasars, which may indicate similar emitting gas properties in the BELR of both types of AGNs. However, a larger sample of Sy1s is obviously needed in order to make a significant comparison.

On the other hand, the mean O I $n(\lambda 11287)/n(\lambda 8446)$ ratio observed in NLS1s is 0.73 ± 0.20 , which is marginally higher than those of quasars and Sy1s (although they agree within the 1σ deviation). This situation is illustrated well in Figure 11, in which we plot the number distributions of the ratio separately for quasars plus Sy1s and for NLS1s. It is direct evidence that radiation-related processes are more efficient over collisional processes in the BELR gas in NLS1s than in quasars and Sy1s. A possible explanation might come from the general idea of the NLS1 containing less massive black holes with higher mass accretion rates, radiating at close to Eddington luminosity (Pounds et al. 1995; Laor et al. 1997a; Mineshige et al. 2000), than normal Seyfert galaxies. Consequently, the line-emitting gas might be exposed to stronger continuum radiation so that the radiation-related processes become predominant. However, in the LOC scenario, the line-emitting region simply moves farther out when the continuum flux is increased at a given radius, so that the incident continuum flux (presumably the ionization parameter) in the region is kept nearly constant. Such a situation is actually confirmed by the reverberation mapping results (Peterson et al. 2002). The difference in the ionizing continuum shape would also not be the origin of the O I $n(\lambda 11287)/n(\lambda 8446)$ difference as we see in §3.3.2; in fact, the O I line ratios predicted in models 3 and 4 are quite similar to each other when the gas density and the ionization parameter are fixed (see Table 7).

Alternatively, the somewhat smaller gas density in the BELR of NLS1 gives a natural explanation for the decreased collisional excitation rate. In this case, the difference in the mean O I $n(\lambda 11287)/n(\lambda 8446)$ ratio between quasars plus Sy1s and the NLS1s corresponds to a few $\times 0.1$ dex smaller gas density in NLS1s, as seen in Figure 7 (*top left*; around the best-fit parameters $\log n_{\text{H}} \sim 11.5$ and $\log U \sim -3.0$).

4.4. Role of the Relevant Gas in the BELR

Our results suggest that a rather high ($n_{\text{H}} \sim 10^{11.5} \text{ cm}^{-3}$) density gas is present in the BELR at the region illuminated by the continuum radiation corresponding to the ionization parameter $U \sim 10^{-2.5}$, producing a dominant part of the observed O I and Ca II emissions. The gas is expected to be located at an outer portion of the BELR. It is a natural consequence of the low ionization potentials of the relevant ions relative to other typical emission lines observed in AGNs and is also indicated by the observed line widths. We list the full widths at half maximum (FWHMs) of the observed C IV $\lambda 1549$ and O I $\lambda 11287$ line profiles in Table 10 as the representatives of the high- and low-ionization lines. These two lines were chosen because they are relatively isolated from other lines and are strong enough to allow reliable measurements. The table shows that the line widths of O I $\lambda 11287$ are 0.3 – 0.5 times

narrower than those of C IV $\lambda 1549$. Assuming that the BELR kinematics is Keplerian so that $V_{\text{FWHM}} \propto r^{-1/2}$, where V_{FWHM} is the emission-line width and r is the distance between the line-emitting gas and the central source (e.g., Peterson & Wandel 1999, 2000), the O I emitting gas seems to be orbiting at a radius several times larger than that of C IV $\lambda 1549$. The reverberation mapping results for the low-ionization lines such as Mg II, Fe II, and H β (Dietrich & Kollatschny 1995; Peterson & Wandel 1999; Vestergaard & Peterson 2005) also support this picture, although the results for the relevant O I and Ca II lines have not been obtained to date.

In order to check the consistency of our results with the observations of other emission lines, we list the calculated EWs of typical UV to optical lines seen in AGNs in Table 11. The calculation was performed with the best-fit (n_{H} , U) parameters to the O I and Ca II observations and the covering factor of 0.1 in the standard model, while similar results were obtained in other models. We also list the EWs measured in a Large Bright Quasar Survey (LBQS) composite spectrum (Francis et al. 1991) for the compared observation. The composite spectrum was constructed from 688 quasars (absolute magnitudes $M_{\text{B}_J} \leq -21.5$) and 30 AGNs (absolute magnitudes $-21.5 \leq M_{\text{B}_J} \leq -20.5$) showing no strong evidence for the presence of broad absorption line troughs (see Foltz et al. 1987; Morris et al. 1991, for details of the observing procedures). The table shows that the O I and Ca II emitting gas exclusively contributes to the permitted low-ionization lines such as Mg II, UV Fe II, and H β , as we expected. On the other hand, a main part of high-ionization lines such as Si IV + O VI] $\lambda 1400$ and C IV $\lambda 1549$ is not produced in this gas; these lines should be formed in an inner portion of the BELR where gas is illuminated by stronger ionizing radiation. The forbidden line [O III] $\lambda 5007$ is also deficient in the emitted spectrum from the gas, which is consistent with the general picture that the line is formed in a much lower density environment in the NELR.

The shape of the Fe II UV bump is correctly reproduced in models 3 and 4, in which v_{turb} is set to 100 km s $^{-1}$ as found by Baldwin et al. (2004). In fact, the best-fit parameters in these models, $(n_{\text{H}}, U) = (10^{12.0} \text{ cm}^{-3}, 10^{-2.5})$, lie on the parameter region consistent with the observed EW and “spike/gap” ratio they defined (see their Fig. 7; our models correspond to $\log n_{\text{H}} = 12.0$ and $\log \Phi_{\text{H}} = 20.0$). Models 1 (the standard model) and 2 cannot reproduce the observed spike/gap ratio; the bump is dominated by the strongest resonance lines, making the predicted ratio much larger than observed. On the other hand, none of the models can reproduce the strong optical Fe II emitters. It has long been a challenge to the photoionized models (e.g., Collin & Joly 2000) and was recently reviewed by Baldwin et al. (2004), who stated that the bulk of the optical Fe II emission might come from a region different from that which produces the UV Fe II emission, such as collisionally ionized gas. We will return to this issue in a forthcoming paper (Tsuzuki et al. 2007).

4.5. Interpretation of the results in the LOC Scenario

In the context of the LOC scenario, an observed spectrum is the sum of emission from the gas at a range of different distances from the central source and also within a range of different densities. Hence the observed emission line flux should be expressed as

$$F_{\text{line}} \propto \int \int r^2 F(r, n_{\text{H}}) f(r) g(n_{\text{H}}) dn_{\text{H}} dr, \quad (2)$$

where $F(r, n_{\text{H}})$ is the emission-line flux of a single cloud at radius r from the central source and with density n_{H} , while $f(r)$ and $g(n_{\text{H}})$ are distribution functions of the gas covering fraction and density, respectively.

In this scenario, the best-fit (n_{H}, U) parameters we derived above correspond to the model producing a dominant part of the observed O I and Ca II emission. We plot the quantity

$$\text{DF}(r, n_{\text{H}}) \equiv r^2 F(r, n_{\text{H}}) f(r) g(n_{\text{H}}) n_{\text{H}} r, \quad (3)$$

for O I $\lambda 8446$ in Figure 12 to see which region on the parameter plane actually dominates the emission. The covering fraction and the gas-density distributions are assumed to be $[f(r) \propto r^0, r^{-1}, r^{-2}]$ and $[g(n_{\text{H}}) \propto n_{\text{H}}^0, n_{\text{H}}^{-1}, n_{\text{H}}^{-2}]$, respectively. With $g(n_{\text{H}}) \propto n_{\text{H}}^0$ or n_{H}^{-2} density distributions, the O I $\lambda 8446$ emission is dominated by much higher or lower density gas than the best-fit model. On the other hand, an $f(r) \propto r^0$ type covering fraction results in dominant emission from the gas that is much farther from the central source (i.e., illuminated by much weaker ionizing radiation) than the best-fit model, while $f(r) \propto r^{-2}$ predicts the opposite end. Thus, the functions of $f(r) \propto r^{-1}$ and $g(n_{\text{H}}) \propto n_{\text{H}}^{-1}$ represent the most plausible distributions of the BELR gas. Note that it is also true in other models (models 2 – 4). It is a consequence of the fact that any of the assumed (n_{H}, U) parameters do not predict the EW of O I lines much greater than observed, i.e., $\text{EW}(\text{O I } \lambda 8446) \gg 10 \text{ \AA}$, with a reasonable covering factor (see Fig. 7, *top right*), so the best-fit parameters are chosen near the EW (O I $\lambda 8446$) maximum on the parameter plane. Since the emission-line flux of a single cloud can be written as $F(r, n_{\text{H}}) = (\text{EW})F_{\text{continuum}} \propto (\text{EW})r^{-2}$, with $f(r) \propto r^{-1}$ and $g(n_{\text{H}}) \propto n_{\text{H}}^{-1}$ distributions, DF becomes

$$\text{DF}(r, n_{\text{H}}) \propto r^2 [(\text{EW})r^{-2}] r^{-1} n_{\text{H}}^{-1} n_{\text{H}} r \propto \text{EW}. \quad (4)$$

It means that the DF distribution is identical to those of EW on the parameter plane so that the best-fit (n_{H}, U) parameters chosen near the EW maximum should also be near the DF maximum. On the other hand, other shapes of $f(r)$ and $g(n_{\text{H}})$ functions predict the DF maxima very differently from that of EW, i.e., very differently from the best-fit (n_{H}, U) parameters. Thus, our results point to the gas distribution of $f(r) \propto r^{-1}$ and $g(n_{\text{H}}) \propto n_{\text{H}}^{-1}$ forms in the LOC model to a first-order approximation.

On the other hand, the DF maximum for the Ca II lines occurs at a much lower value of U than the best-fit (n_{H} , U) parameters with $f(r) \propto r^{-1}$ and $g(n_{\text{H}}) \propto n_{\text{H}}^{-1}$ distribution functions, as shown in Figure 13. It implies that the gas distribution should have a cutoff somewhere around $U \sim 10^{-3.5}$ at $n_{\text{H}} = 10^{11.0} - 10^{12.0} \text{ cm}^{-3}$, which should originate from the physical nature of the BELR. In fact, Baldwin et al. (1995) constrained a range of the LOC integration over the parameter space to $\Phi > 10^{18} \text{ s}^{-1} \text{ cm}^{-2}$, since gas at a larger distance than this limit will form graphite grains (Sanders et al. 1989) so that the line emission is heavily suppressed (Netzer & Laor 1993). This limit corresponds to $U \gtrsim 10^{-3.5}$ at $n_{\text{H}} = 10^{11.5} \text{ cm}^{-3}$, which is consistent with the above expectation.

5. SUMMARY

We present results of the near-IR spectroscopy of six quasars with redshifts ranging from 0.158 to 1.084. Combined with the UV data taken with the *HST* FOS, we give the relative strengths of O I $\lambda 1304$, O I $\lambda 8446$, O I $\lambda 11287$, and the Ca II triplet ($\lambda 8498$, $\lambda 8542$, and $\lambda 8662$). Detailed model calculations were performed in the framework of the photoionized BELR gas for a wide range of physical parameters and compared to the observations, which led us to the following conclusions.

1. A rather dense gas with density $n_{\text{H}} \sim 10^{11.5} \text{ cm}^{-3}$ is present at an outer portion of the BELR, whose distance from the central source corresponds to the ionization parameter $U \sim 10^{-2.5}$. The gas is primarily responsible for the observed O I, Ca II, and Fe II lines based on the resemblance of their profiles.
2. The strongest O I lines observed in typical AGN spectra, i.e., $\lambda 1304$, $\lambda 8446$, and $\lambda 11287$, are formed through Ly β fluorescence and collisional excitation. It is consistent with the absence or weakness of other O I lines such as $\lambda 7774$ and $\lambda 13165$.
3. The fractions of the O I $\lambda 1304$ triplet and the Si II $\lambda 1308$ doublet blended in the $\lambda 1304$ bump typically seen in AGN spectra vary from quasar to quasar, ranging from 20% to 60% in the O I fraction. Such a large flux in the Si II doublet might be accounted for by the LOC-type integration over the gas physical parameter space or by an unusually large microturbulent velocity.
4. The flux ratio between O I $\lambda 8446$ and $\lambda 11287$ observed in Sy1s may indicate that the physical condition within the line-emitting gas is similar to those in quasars. On the other hand, the ratios observed in NLS1s suggest that radiation-related processes are more efficient over collisional processes than in quasars and Sy1s. It might be a consequence of a stronger continuum radiation incident on the line-emission region, or lower gas density in NLS1s.

5. In the LOC scenario, the revealed physical parameters of the line-emitting gas should represent the maximum contribution to the observed O I and Ca II emission in the parameter space. Such a condition requires the distribution functions of the gas covering fraction and the density of $f(r) \propto r^{-1}$ and $g(n_{\text{H}}) \propto n_{\text{H}}^{-1}$, respectively.

We are grateful to an anonymous referee for giving a number of useful comments to improve this paper. G. J. Ferland kindly gave us the useful advices regarding the photoionization code Cloudy. We thank the staff of UKIRT for technical support and assistance with the observation. Use of the UKIRT is supported by the National Astronomical Observatory of Japan. This work has been supported in part by Grants-in-Aid for Scientific Research (15253002, 17104002) and the Japan-Australia Research Cooperative Program from the Japan Society for the Promotion of Science.

REFERENCES

Baldwin, J. A., Ferland, G. J., Korista, K. T., Carswell, R. F., Hamann, F., Phillips, M. M., Verner, D., Wilkes, B. J., & Williams, R. E. 1996, ApJ, 461, 664

Baldwin, J. A., Ferland, G. J., Korista, K. T., Hamann, F., & LaCluyzé, A. 2004, ApJ, 615, 610

Baldwin, J. A., Ferland, G. J., Korista, K. T., & Verner, D. 1995, ApJ, 455, L119

Binette, L., Prieto, A., Szuszkiewicz, E., & Zheng, W. 1989, ApJ, 343, 135

Bottorff, M., & Ferland, G. J. 2000, MNRAS, 316, 103

Bottorff, M., Ferland, G., Baldwin, J., & Korista, K. 2000, ApJ, 542, 644

Cheng, F. H., Gaskell, C. M., & Koratkar, A. P. 1991, ApJ, 370, 487

Collin, S., & Joly, M. 2000, New A Rev., 44, 531

Constantin, A., Shields, J. C., Hamann, F., Foltz, C. B., & Chaffee, F. H. 2002, ApJ, 565, 50

Davidson, K., & Netzer, H. 1979, Rev. Mod. Phys., 51, 715

Dietrich, M., & Kollatschny, W. 1995, A&A, 303, 405

Dietrich, M., Appenzeller, I., Vestergaard, M., & Wagner, S. J. 2002, ApJ, 564, 581

Dietrich, M., Hamann, F., Appenzeller, I., & Vestergaard, M. 2003, *ApJ*, 596, 817

De Zotti, G., & Gaskell, C. M. 1985, *A&A*, 147, 1

Elston, R., Thompson, K. L., & Hill, G. J. 1994, *Nature*, 367, 250

Evans, I. N., & Koratkar, A. P. 2004, *ApJS*, 150, 73

Ferland, G. J. 2004, Hazy 2, A brief introduction to Cloudy 96 – computational methods, 288

Ferland, G. J., Korista, K. T., Verner, D. A., Ferguson, J. W., Kingdon, J. B., & Verner, E., M. 1998, *PASP*, 110, 761

Ferland, G. J., & Persson, S. E. 1989, *ApJ*, 347, 656

Foltz, C. B., Chaffee, F. H., Hewett, P. C., MacAlpine, G. M., Turnshek, D. A., Weymann, R. J., & Anderson, S. F. 1987, *AJ*, 94, 1423

Francis, P. J., Hewett, P. C., Foltz, C. B., Chaffee, F. H., Weymann, R. J., & Morris, S. L. 1991, *ApJ*, 373, 465

Freudling, W., Corbin, M. R., & Korista, K. T. 2003, *ApJ*, 587, L67

Glikman, E., Helfand, D. J., & White, R. L. 2006, *ApJ*, 640, 579

Grandi, S. A. 1975a, *ApJ*, 196, 465

Grandi, S. A. 1975b, *ApJ*, 199, L43

Grandi, S. A. 1980, *ApJ*, 238, 10

Grandi, S. A. 1983, *ApJ*, 268, 591

Hamann, F., & Ferland, G. 1993, *ApJ*, 418, 11

Hamann, F., & Ferland, G. 1999, *ARA&A*, 37, 487

Hawarden, T. G., Leggett, S. K., Letawsky, M. B., Ballantyne, D. R., & Casali, M. M. 2001, *MNRAS*, 325, 563

Hopkins, P. F., et al. 2004, *AJ*, 128, 1112

Iwamuro, F., Kimura, M., Eto, S., Maihara, T., Motohara, K., Yoshii, Y., & Doi, M. 2004, *ApJ*, 614, 69

Iwamuro, F., Motohara, K., Maihara, T., Kimura, M., Yoshii, Y., & Doi, M. 2002, ApJ, 565, 63

Kawara, K., Murayama, T., Taniguchi, Y., & Arimoto, N. 1996, ApJ, 470, L85

Königl, A., & Kartje, J. F. 1994, ApJ, 434, 446

Korista, K., Baldwin, J., Ferland, G., & Verner, D. 1997, ApJS, 108, 401

Krolik, J. H., & Kallman, T. R. 1988, ApJ, 324, 714

Kwan, J., & Krolik, J. H. 1981, ApJ, 250, 478

Laor, A., Fiore, F., Elvis, M., Wilkes, B. J., & McDowell, J. C. 1997a, ApJ, 477, 93

Laor, A., Jannuzzi, B. T., Green, R. F., & Boroson, T. A. 1997b, ApJ, 489, 656

Leggett, S. K., Currie, M. J., Varricatt, W. P., Hawarden, T. G., Adamson, A. J., Buckle, J., Carroll, T., Davies, J. K., Davis, C. J., Kerr, T. H., Kuhn, O. P., Seigar, M. S., & Wold, T. 2006, MNRAS, 373, 781

Maiolino, R., Juarez, Y., Mujica, R., Nagar, N. M., & Oliva, E. 2003, ApJ, 596, L155

Matsuoka, Y., Oyabu, S., Tsuzuki, Y., Kawara, K., & Yoshii, Y. 2005, PASJ, 57, 563

Mineshige, S., Kawaguchi, T., Takeuchi, M., & Hayashida, K. 2000, PASJ, 52, 499

Morris, S. L., Weymann, R. J., Anderson, S. F., Hewett, P. C., Francis, P. J., Foltz, C. B., Chaffee, F. H., & MacAlpine, G. M. 1991, AJ, 102, 1627

Netzer, H., & Laor, A. 1993, ApJ, 404, L51

Netzer, H., & Wills, B. J. 1983, ApJ, 275, 445

O'Brien, P. T., Goad, M. R., & Gondhalekar, P. M. 1995, MNRAS, 275, 1125

Pei, Y. C. 1992, ApJ, 395, 130

Péquignot, D., Petitjean, P., & Boisson, C. 1991, A&A, 251, 680

Persson, S. E. 1988, ApJ, 330, 751

Peterson, B. M., & Wandel, A. 1999, ApJ, 521, L95

Peterson, B. M., & Wandel, A. 2000, ApJ, 540, L13

Peterson, B. M., et al. 2002, *ApJ*, 581, 197

Pounds, K. A., Done, C., & Osborne 1995, *MNRAS*, 277, L5

Ramsay Howatt, S. K., et al. 2004, *Proc. SPIE*, 5492, 1160

Rees, M. J. 1987, *MNRAS*, 228, 47

Riffel, R., Rodríguez-Ardila, A., & Pastoriza, M. G. 2006, *A&A*, 457, 61

Rodríguez-Ardila, A., Viegas, S. M., Pastoriza, M. G., & Prato, L. 2002a, *ApJ*, 565, 140

Rodríguez-Ardila, A., Viegas, S. M., Pastoriza, M. G., Prato, L., & Donzelli, C. J. 2002b, *ApJ*, 572, 94

Rudy, R. J., Erwin, P., Rossano, G. S., & Puetter, R. C. 1991, *ApJ*, 383, 344

Rudy, R. J., Mazuk, S., Puetter, R. C., & Hamann, F. 2000, *ApJ*, 539, 166

Rudy, R. J., Rossano, G. S., & Puetter, R. C. 1989, *ApJ*, 342, 235

Sanders, D. B., Phinney, E. S., Neugebauer, G., Soifer, B. T., & Matthews, K. 1989, *ApJ*, 347, 29

Schlegel, D. J., Finkbeiner, D. P., & Davis, M. 1998, *ApJ*, 500, 525

Sigut, T. A. A., & Pradhan, A. K. 1998, *ApJ*, 499, L139

Sigut, T. A. A., & Pradhan, A. K. 2003, *ApJS*, 145, 15

Tsuzuki, Y., Kawara, K., Yoshii, Y., Oyabu, S., Tanabé, T., & Matsuoka, Y. 2006, *ApJ*, 650, 57

Tsuzuki, Y., et al. 2007, in preparation

Verner, D. A., Verner, E. M., & Ferland, G. J. 1996, *Atomic Data Nucl. Data Tables*, 64, 1

Verner, E., Bruhweiler, F., Verner, D., Johansson, S., & Gull, T. 2003, *ApJ*, 592, L59

Verner, E. M., Verner, D. A., Korista, K. T., Ferguson, J. W., Hamann, F., & Ferland, G. J. 1999, *ApJS*, 120, 101

Véron-Cetty, M.-P., & Véron, P. 2003, *A&A*, 412, 399

Vestergaard, M., & Peterson, B. M. 2005, *ApJ*, 625, 688

Wills, B. J., Netzer, H., & Wills, D. 1985, *ApJ*, 288, 94

Yoshii, Y., Tsujimoto, T., & Kawara, K. 1998, *ApJ*, 507, L113

Zheng, W., Kriss, G. A., Davidson, A. F., Lee, G., Code, A. D., Bjorkman, K. S., Smith, P. S., Weistrop, D., Malkan, M. A., Baganoff, F. K., & Peterson, B. M. 1995, *ApJ*, 444, 632

Table 1: Characteristics of the Observed Quasars

Object	Redshift ^a	M_B ^b	A_V ^c	J (2MASS) ^d	H (2MASS) ^d	J ^e	H ^e
3C 273	0.158	−26.9	0.007	11.8	11.0	11.5	...
QSO B0850+440	0.514	−26.1	0.011	15.2	14.4	...	15.0
3C 232	0.530	−26.7	0.005	14.9	14.4	...	14.4
QSO J1139−1350	0.560	−26.3	0.013	15.5	14.9	...	15.0
PG 1148+549	0.978	−27.7	0.004	14.5	14.2	...	14.6
PG 1718+481	1.084	−29.8	0.006	13.5	13.0	...	13.0

^aRedshift measured in the UV spectra (Evans & Koratkar 2004).

^bThe B -band absolute magnitude taken from Véron-Cetty & Véron (2003).

^cGalactic extinction (Schlegel et al. 1998); $R_V = 3.08$ was adopted (Pei 1992).

^dThe J - and H -band magnitudes measured in the 2MASS observations.

^eThe J - and H -band magnitudes measured in this work.

Table 2: Observing Journal of the Near-IR Spectroscopy

Target	Exposure Time (s)	Grism	Air Mass	Rationing Star
3C 273	2400	IJ	1.1	BS 4708 (F8V)
QSO B0850+440	3840	JH	1.5	BS 3451 (F7V)
3C 232	7680	JH	1.2	BS 3625 (F9V)
QSO J1139−1350	6720	JH	1.3	BS 4529 (F7V)
PG 1148+549	2880	HK	1.2	BS 4761 (F7V)
PG 1718+481	1920	HK	1.5	BS 6467 (F4V)

Table 3: Observing Journal of the Near-IR Imaging

Target	Exposure Time (s)	Filter	Air Mass	Standard Star
3C 273	50	J	1.1	FS 132
QSO B0850+440	300	H	1.3	FS 125
3C 232	300	H	1.6	FS 127
QSO J1139−1350	300	H	1.6	FS 129
PG 1148+549	300	H	1.2	FS 121
PG 1718+481	150	H	1.6	FS 141

Table 4. Measured Emission-Line Fluxes^a

Emission Lines	3C 273	QSO B0850+440	3C 232	QSO J1139–1350	PG 1148+549	PG 1718+481
UV Lines						
Ly β + O VI λ 1030	2530 \pm 140	160 \pm 24	...	123 \pm 10	97.1 \pm 9.9	123 \pm 9
Ly α + N V λ 1220	19600 \pm 200	711 \pm 26	457 \pm 16	1030 \pm 20	1200 \pm 20	2070 \pm 30
Si II λ 1264	53.5 \pm 11.2	5.88 \pm 0.55	3.60 \pm 1.66	<7.7	14.4 \pm 6.3	25.6 \pm 2.3
O I + Si II λ 1304	404 \pm 50	24.3 \pm 3.0	24.7 \pm 3.0	19.2 \pm 2.0	37.3 \pm 4.2	45.0 \pm 8.2
C II λ 1335	...	10.2 \pm 1.3	9.94 \pm 1.12	7.01 \pm 1.68	24.1 \pm 3.2	20.3 \pm 3.7
Si IV + O VI] λ 1400	...	70.1 \pm 3.4	41.1 \pm 2.36	68.6 \pm 7.4	101 \pm 6	174 \pm 14
C IV λ 1549	7400 \pm 140	263 \pm 7	165 \pm 6	578 \pm 7	216 \pm 8	196 \pm 31
C III] λ 1909	1680 \pm 90	112 \pm 7	128 \pm 5	51.9 \pm 3.3
Near-IR Lines						
O I λ 8446	239 \pm 26	5.07 \pm 1.17	0.98 \pm 0.17	4.31 \pm 0.77	8.10 \pm 0.26	9.62 \pm 1.05
Ca II λ 8579 ^b	343 \pm 31	8.15 \pm 1.83	<0.39	2.08 \pm 0.59	9.40 \pm 0.29	10.5 \pm 1.7
Pa ϵ +[S III] λ 9540	228 \pm 12	4.49 \pm 0.54	5.61 \pm 0.20	5.60 \pm 0.47	6.51 \pm 0.35	...
Pa δ + Fe II λ 10050	302 \pm 7	5.38 \pm 0.37	2.35 \pm 0.22	10.5 \pm 0.8	9.01 \pm 0.29	17.3 \pm 0.48
Fe II λ 10501	...	1.95 \pm 0.28	...	1.25 \pm 0.35	0.99 \pm 0.13	...
He I λ 10830	499 \pm 20	14.2 \pm 1.4	15.0 \pm 1.3	23.2 \pm 3.6	23.9 \pm 13.1	25.6 \pm 1.9
Pa γ λ 10941	402 \pm 20	4.52 \pm 1.15	9.76 \pm 1.27	11.5 \pm 3.6	16.5 \pm 13.1	35.9 \pm 2.1
O I λ 11287	59.4 \pm 1.2	2.34 \pm 0.20	1.29 \pm 0.57	0.77 \pm 0.11	1.99 \pm 0.10	3.41 \pm 0.76

^aThe fluxes are given in units of 10^{-15} erg s $^{-1}$ cm $^{-2}$.

^bTotal flux of the near-IR Ca II triplet (λ 8498, λ 8542, and λ 8662).

Table 5. O I and Ca II Line Strengths Used to Constrain the Models

Object	EW (O I λ 8446) (Å)	$O\ I\ n(\lambda 11287)/n(\lambda 8446)$	$n(\text{Ca II})/n(\text{O I } \lambda 8446)$ ^a	References ^b
Quasar				
3C 273	19.9	0.33 ± 0.04	1.46 ± 0.21	This work
QSO B0850+440	37.7	0.62 ± 0.15	1.63 ± 0.53	This work
3C 232 ^c	2.7	1.76 ± 0.83	< 0.40	This work
QSO J1139–1350	25.0	0.24 ± 0.05	0.49 ± 0.16	This work
PG 1148+549	51.5	0.33 ± 0.02	1.18 ± 0.05	This work
PG 1718+481	15.9	0.47 ± 0.12	1.11 ± 0.22	This work
PG 1116+215	23.8	0.76 ± 0.27	...	1
Sy1				
NGC 863	...	0.55 ± 0.08	...	2
NLS1				
1H 1934–063	...	0.64 ± 0.05	...	2
Ark 564	...	0.82 ± 0.03	...	2
Mrk 335	...	0.64 ± 0.05	...	2
Mrk 1044	...	0.42 ± 0.05	...	2
Ton S180	...	1.08 ± 0.16	...	2
I Zw 1	...	0.76 ± 0.11	...	3, 4

^aThe representative wavelength of 8579 Å was used to convert the Ca II triplet flux to the photon number flux.

^bReferences — (1) Matsuoka et al. (2005). (2) Rodríguez-Ardila et al. (2002b). (3) Laor et al. (1997b). (4) Rudy et al. (2000).

^cThis quasar is excluded from the sample to be compared with the model calculations, due to its anomalously weak O I λ 8446 emission.

Table 6: Input Parameters of the Photoionized Models

Model	Continuum Shape	v_{turb} (km s $^{-1}$)
	$(T_{\text{cut}} [\text{K}], \alpha_{\text{uv}}, \alpha_{\text{x}}, \alpha_{\text{ox}})^{\text{a}}$	
1 (standard)	$(1.5 \times 10^5, -0.2, -1.8, -1.4)$	0
2	$(1.5 \times 10^5, -0.2, -1.8, -1.4)$	10
3	$(1.5 \times 10^5, -0.2, -1.8, -1.4)$	100
4	$(1.0 \times 10^6, -0.5, -1.0, -1.4)$	100

^aSee text for the definition of these parameters.

Table 7: Results of the Photoionized Model Calculations and the Compared Observation

Parameter/Prediction	Model 1	Model 2	Model 3	Model 4	Observed
Best-Fit Parameter					
n_{H} (cm $^{-3}$)	$10^{11.5}$	$10^{11.5}$	$10^{12.0}$	$10^{12.0}$	N/A
U	$10^{-3.0}$	$10^{-2.5}$	$10^{-2.5}$	$10^{-2.5}$	N/A
Predicted Line Strengths					
EW (O I $\lambda 8446$) ^a	12.0	12.1	8.72	5.08	> 10
O I $n(\lambda 11287)/n(\lambda 8446)$	0.56	0.58	0.52	0.53	0.46 ± 0.18
O I $n(\lambda 1304)/n(\lambda 8446)$	0.45	0.48	0.40	0.41	...
$n(\text{Ca II})/n(\text{O I } \lambda 8446)$	2.51	1.57	0.95	1.04	0.1 - 5.0

^aThe EWs are computed with a covering factor of 0.1 and given in units of angstroms.

Table 8. Observed and Theoretical Values of the O I Line Ratios

Object	type	$\lambda7254/\lambda8446$	$\lambda7774/\lambda8446$	$\lambda7990/\lambda8446$	$\lambda13165/\lambda11287$	References ^a
Observed						
NGC 4151	Sy1	≤ 0.08	≤ 0.02	≤ 0.04	...	1
NGC 5548	Sy1	≤ 0.05	≤ 0.06	≤ 0.02	...	1
Mrk 42	Sy1	≤ 0.03	≤ 0.08	≤ 0.03	...	1
Mrk 335	Sy1	≤ 0.01	≤ 0.04	≤ 0.02	...	1
Akn 564	Sy1	≤ 0.04	≤ 0.03	≤ 0.02	...	1
1H 1934–063	NLS1	< 0.03	0.07	0.04	< 0.02	2
Ark 564	NLS1	< 0.07	2
Mrk 335	NLS1	< 0.05	2
Mrk 1044	NLS1	< 0.14	2
Ton S180	NLS1	...	< 0.08	< 0.09	...	2
Theoretical Predictions						
Ly β fluorescence		0.0	0.0	0.0	0.0	—
Collisional excitation		...	0.3 ^b	1
Continuum fluorescence		0.025	...	0.052	~ 1.0	1
Recombination		...	7.2 ^c	This work

^aReferences — (1) Grandi (1980). (2) Rodríguez-Ardila et al. (2002b).

^bOnly the collisional cross sections from the ground term are considered (see text).

^cAppropriate in the low-density limit (e.g., in the normal Galactic gaseous nebulae).

Table 9: Constitution of the $\lambda 1304$ Bump^a

Object	O I ^b	Si II
3C 273	264 (0.65) – 396 (0.98)	8 – 140
QSO B0850+440	15.3 (0.63) – 18.5 (0.76)	5.8 – 9.0
QSO J1139–1350	1.7 (0.09) – 4.1 (0.21)	15.1 – 17.5
PG 1148+549	7.8 (0.21) – 12.6 (0.34)	24.7 – 29.5
PG 1718+481	19.8 (0.44) – 25.4 (0.56)	19.6 – 25.2

^aFluxes are given in units of 10^{-15} ergs s^{-1} cm^{-2} , as in Table 4.

^bValues in parentheses represent the fractions in the bump.

Table 10: Measured FWHMs of the C IV $\lambda 1549$ and O I $\lambda 11287$ Lines

Object	C IV $\lambda 1549$	O I $\lambda 11287$
3C 273	3940	2160
QSO B0850+440	5540	1960
3C 232	7430	2410
QSO J1139–1350	3790	1210
PG 1148+549	5860	1830
PG 1718+481	3720	1840

Note — The FWHMs are given in units of kilometers per second.

Table 11: Equivalent Widths of the Typical UV and Optical Emission Lines

Line	Model ^a	Observed ^b
Ly α λ 1216 + N V λ 1240	40.8	52
Si IV+O VI] λ 1400	0.49	10
C IV λ 1549	1.35	37
C III] λ 1909	0.23	22
Fe II $\lambda\lambda$ 2240 – 2650	16.7	49
Mg II λ 2800	65.0	50
H β λ 4863	31.0	58
[O III] λ 5007	0.0020	15

Note — Equivalent widths are given in units of angstroms.

^aThe standard model with the best-fit (n_{H} , U) parameters to the O I and Ca II observations and a covering factor of 0.1.

^bThe EWs of Emission lines in the LBQS composite spectrum were taken from Francis et al. (1991), except for that of the Fe II, which was taken from Baldwin et al. (2004).

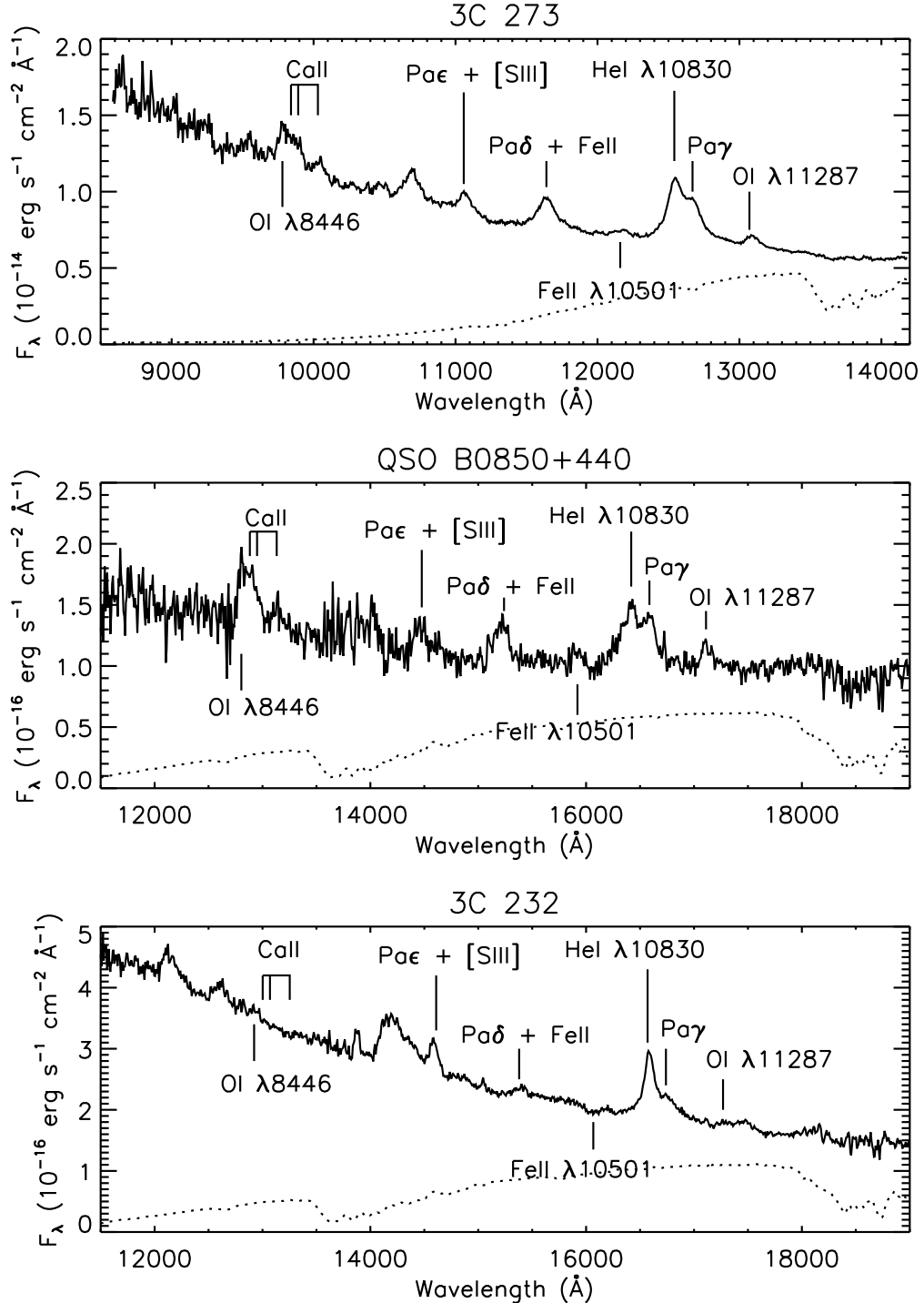


Fig. 1.— Reduced near-IR spectra (*solid lines*) along with the sensitivity curves (with arbitrary amounts of scaling; *dotted lines*) for 3C 273, QSO B0850+440, and 3C 232 in the observed frame. Positions of the identified emission lines are marked with vertical lines.

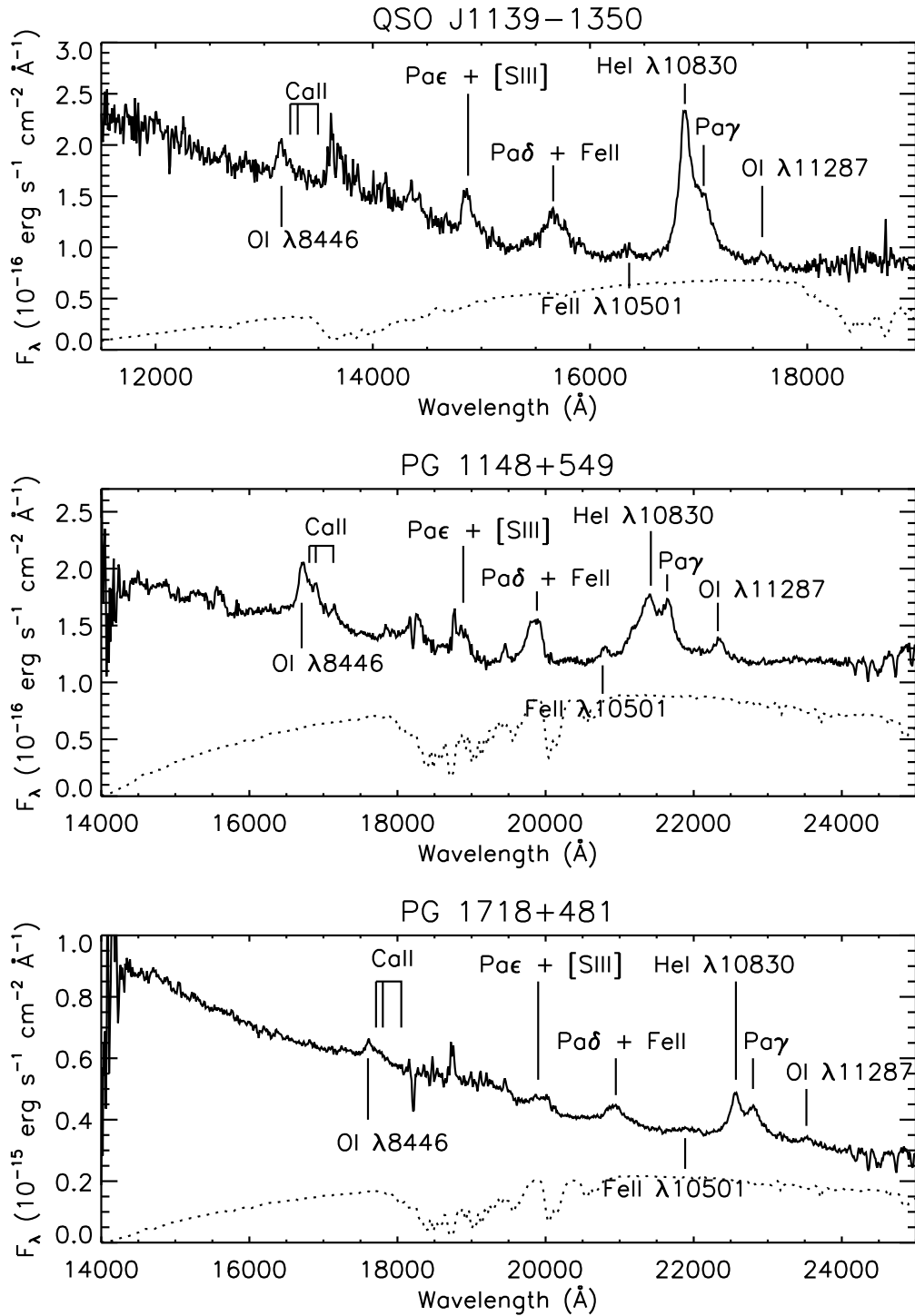


Fig. 2.— Same as Fig. 1 but for QSO J1139–1350, PG 1148+549, and PG 1718+481.

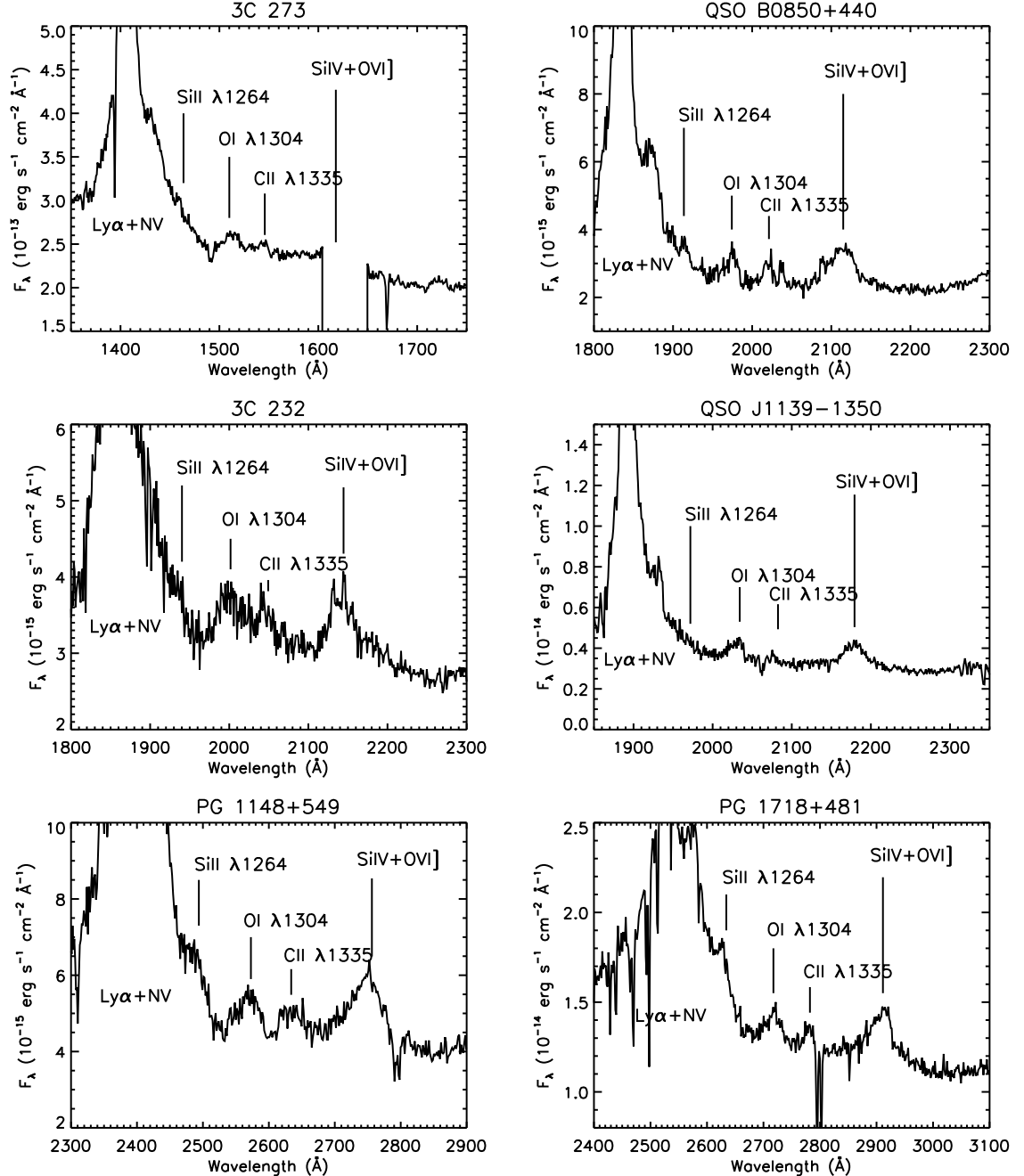


Fig. 3.— UV spectra around O I $\lambda 1304$ for 3C 273, QSO B0850+440, 3C 232, QSO J1139–1350, PG 1148+549, and PG 1718+481 in the observed frame. Positions of the identified emission lines are marked with vertical lines.

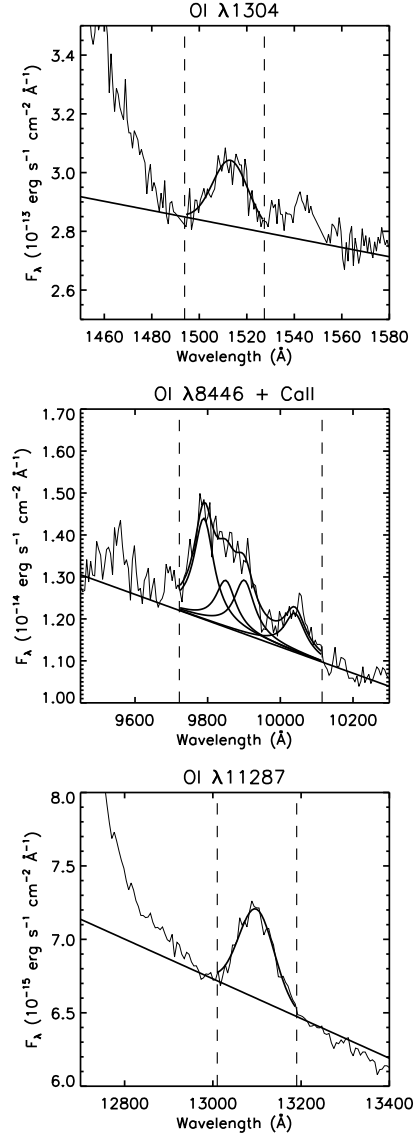


Fig. 4.— Fitting results for O I λ 1304, O I λ 8446 + the Ca II triplet (λ 8498, λ 8542, and λ 8662), and O I λ 11287 in 3C 273. Observed spectra are shown by thin solid lines while the determined continuum and the fitted Voigt profiles are shown by thick solid lines. The sum of these fitted components are also shown by a thick solid line for O I λ 8446 + the Ca II triplet. The wavelength ranges used in the fitting are indicated by vertical dashed lines.

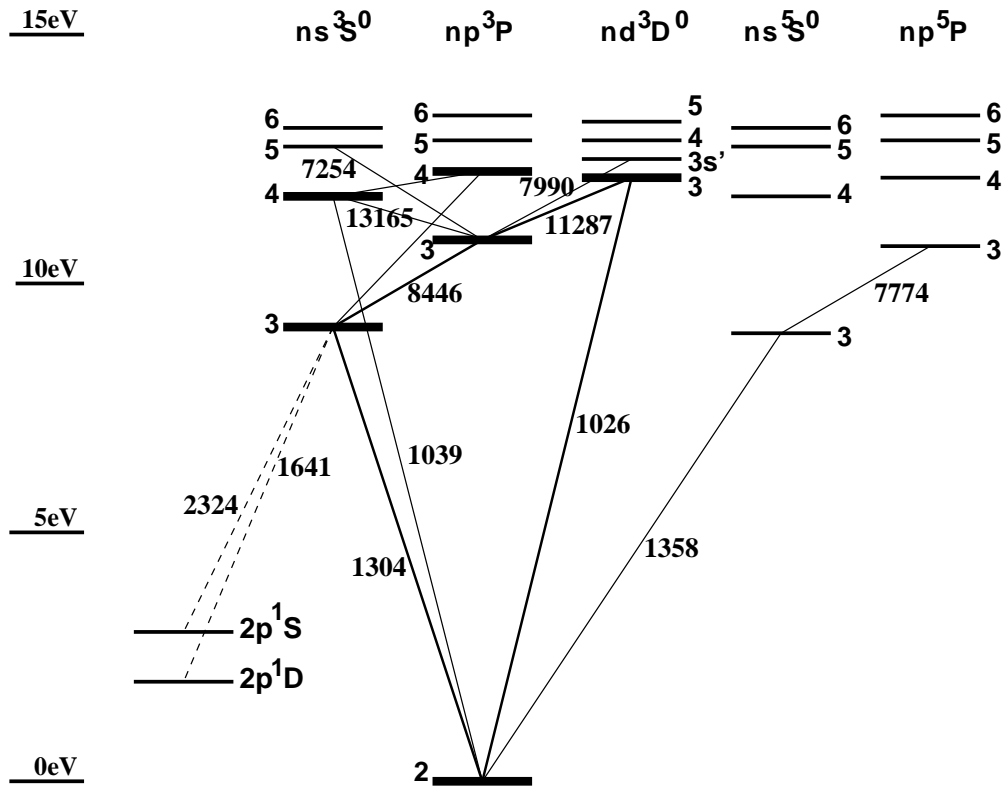


Fig. 5.— Partial Grotrian diagram of an O I atom. Solid lines represent permitted transitions, while dashed lines represent semi-forbidden transitions. Transition paths of the Ly β -pumped electrons (corresponding to $\lambda 1026$, $\lambda 11287$, $\lambda 8446$, and $\lambda 1304$) are shown by thick solid lines. The six energy levels considered in the model calculations are shown by thick horizontal lines.

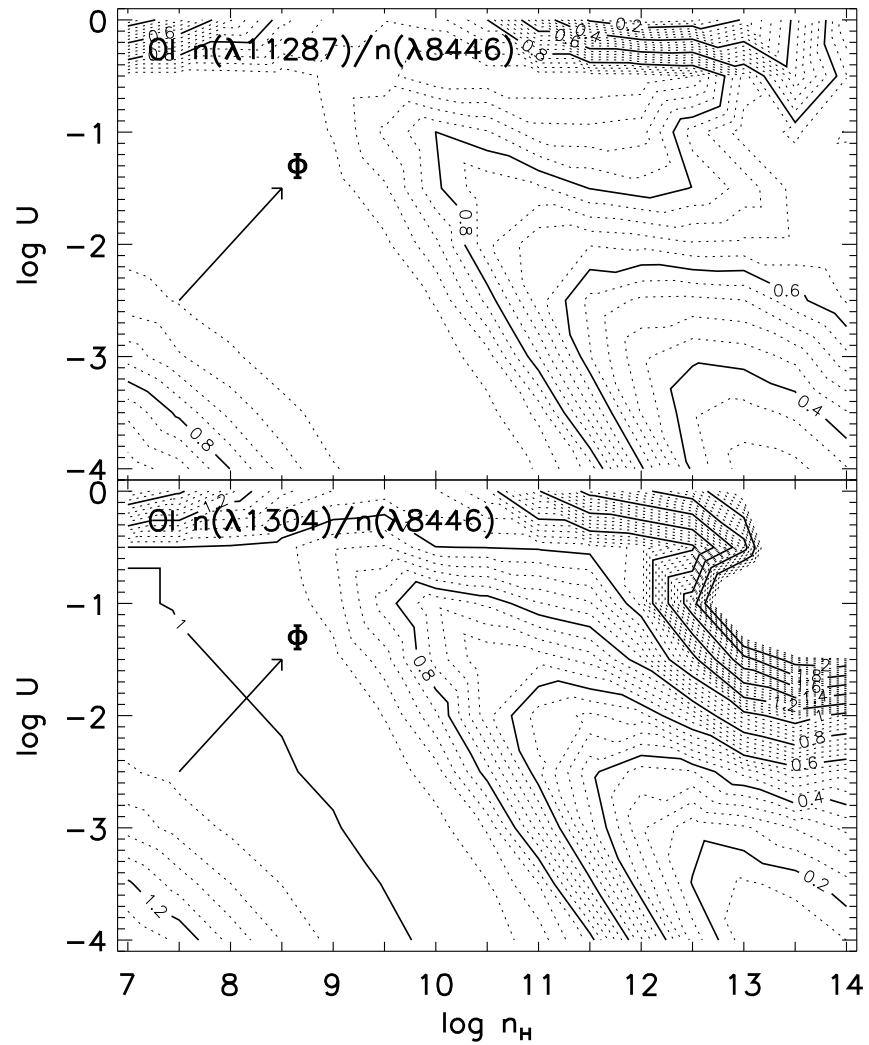


Fig. 6.— O I photon flux ratios $n(\lambda 11287)/n(\lambda 8446)$ (top) and $n(\lambda 1304)/n(\lambda 8446)$ (bottom) as a function of the gas density n_{H} and the ionization parameter U , calculated in the standard model. The contours are linearly spaced. Arrows indicate the direction toward which the incident-ionizing continuum flux Φ increases.

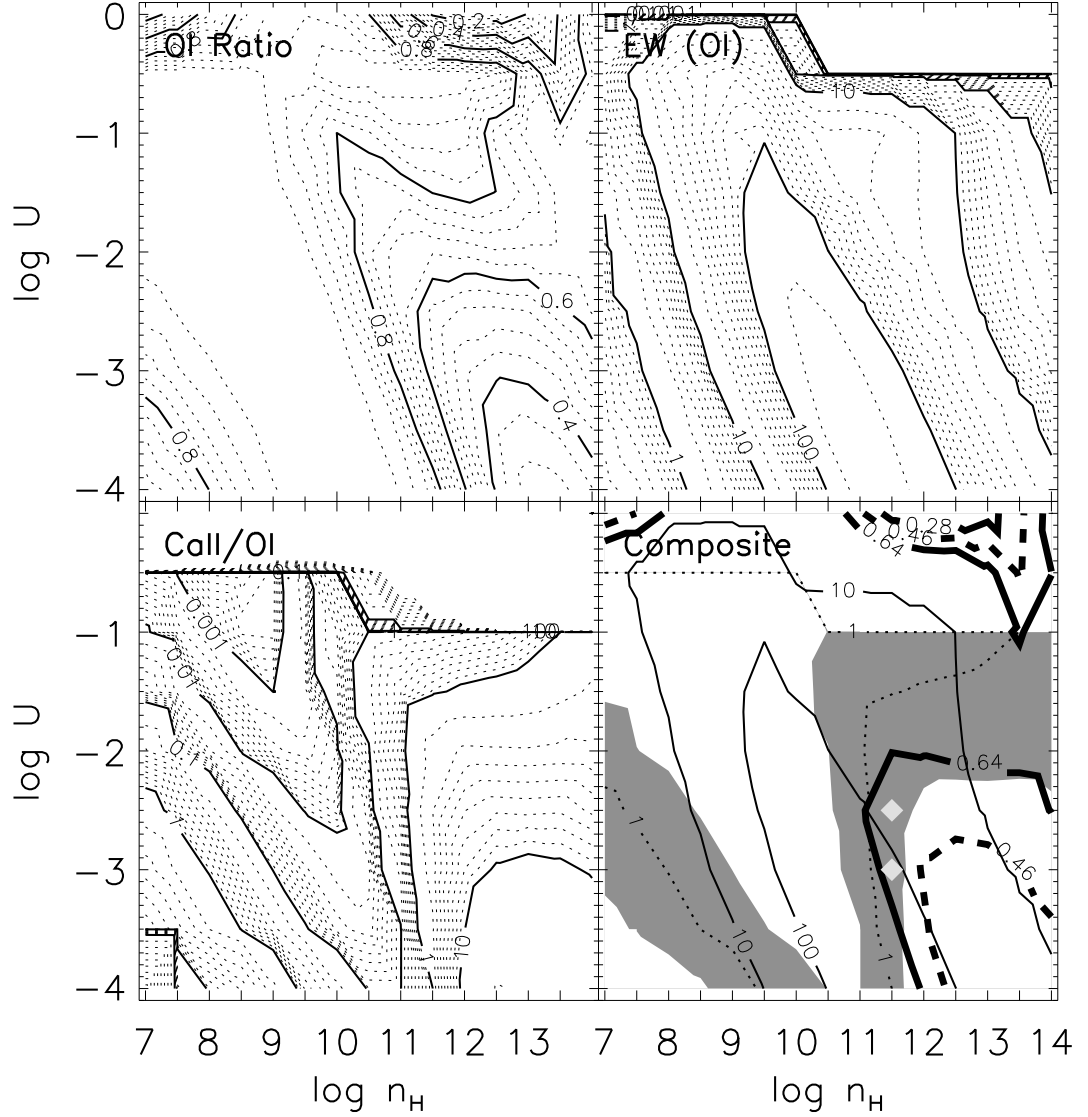


Fig. 7.— $\text{O I } n(\lambda 11287)/n(\lambda 8446)$ (top left), $\text{EW} (\text{O I } \lambda 8446)$ in units of angstroms (top right), $n(\text{Ca II})/n(\text{O I } \lambda 8446)$ (bottom left), and their composite plot (bottom right) as a function of the gas density n_H and the ionization parameter U , calculated in the standard model. In the bottom right panel, the three constraints from the observed $\text{O I } n(\lambda 11287)/n(\lambda 8446)$, $\text{EW} (\text{O I } \lambda 8446)$, and $n(\text{Ca II})/n(\text{O I } \lambda 8446)$ values are shown by thick solid lines, thin solid lines, and the shaded area, respectively. The models consistent with all the constraints are marked with diamonds. Dashed lines and dotted lines represent mean values of the observed $\text{O I } n(\lambda 11287)/n(\lambda 8446)$ and $n(\text{Ca II})/n(\text{O I } \lambda 8446)$, respectively. Note that the contours in the top left panel are linearly spaced, while they are spaced logarithmically in the top right and the bottom left panels.

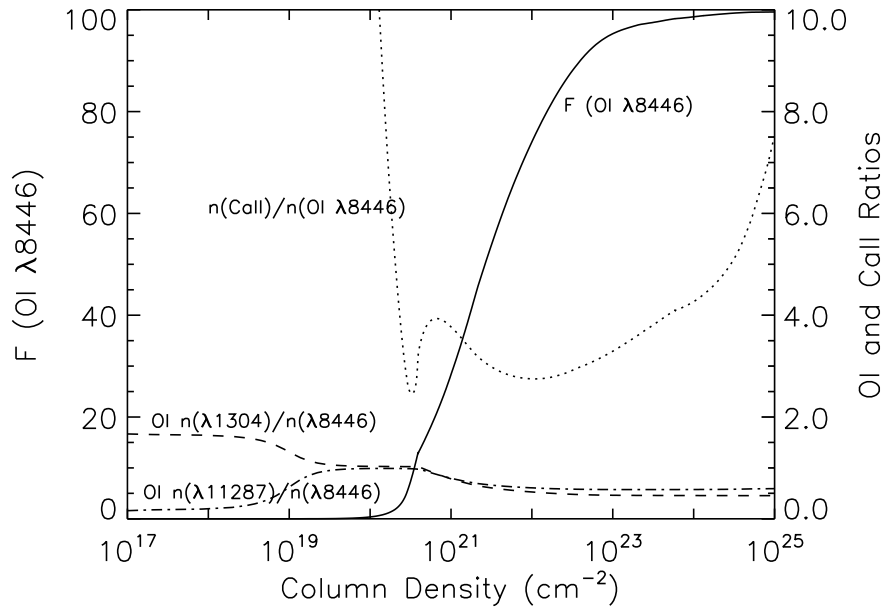


Fig. 8.— Cumulative flux of O I $\lambda 8446$ (with an arbitrary scaling; *solid line*) and ratios of O I $n(\lambda 1304)/n(\lambda 8446)$, O I $n(\lambda 11287)/n(\lambda 8446)$, and $n(\text{Ca II})/n(\text{O I } \lambda 8446)$ (*dashed line*, *dot-dashed line*, and *dotted line*, respectively), plotted against the gas column density measured from the illuminated surface. The model parameters other than the column density N_{H} used in the calculation are identical to those of the standard model with $(n_{\text{H}}, U) = (10^{11.5} \text{ cm}^{-3}, 10^{-3.0})$.

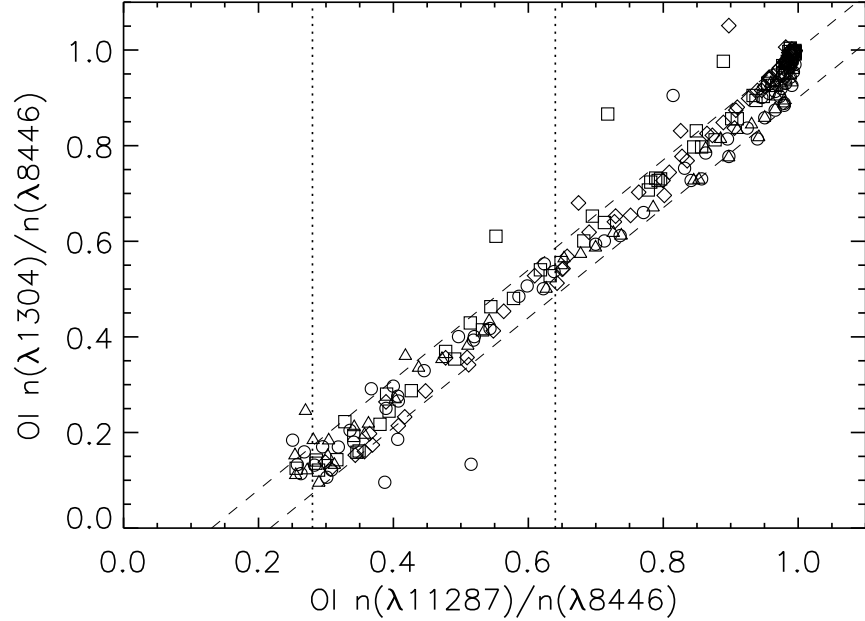


Fig. 9.— O I photon flux ratios $n(\lambda 11287)/n(\lambda 8446)$ vs. $n(\lambda 1304)/n(\lambda 8446)$ calculated in models 1 – 4 with the (n_{H}, U) parameters around the best-fit values, with which the O I line formation is dominated by Ly β fluorescence and collisional excitation (see text). Diamonds represent model 1 with different (n_{H}, U) parameter values, while squares represent model 2, circles represent model 3, and triangles represent model 4. Dotted lines show a range of the observed values, $n(\lambda 11287)/n(\lambda 8446) = 0.46 \pm 0.18$. We regard the $n(\lambda 1304)/n(\lambda 8446)$ values enclosed by two dashed lines, drawn to include most of the points in the observed $n(\lambda 11287)/n(\lambda 8446)$ range, as allowed values given the $n(\lambda 11287)/n(\lambda 8446)$ ratio.

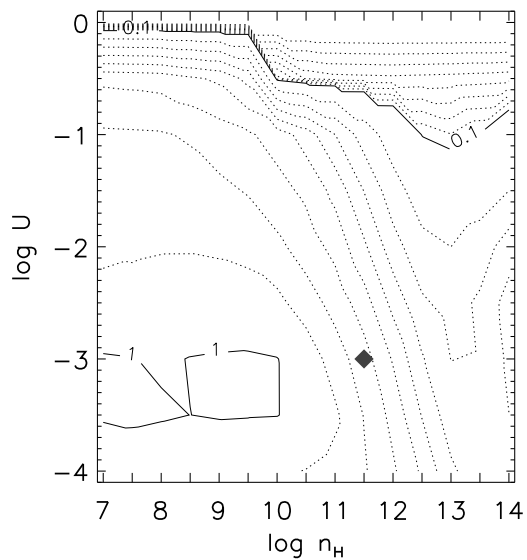


Fig. 10.— EWs of the Si II $\lambda 1308$ doublet in units of angstroms, as a function of the gas density n_H and the ionization parameter U calculated in the standard model. A diamond represents the best-fit parameters to the O I and Ca II observations.

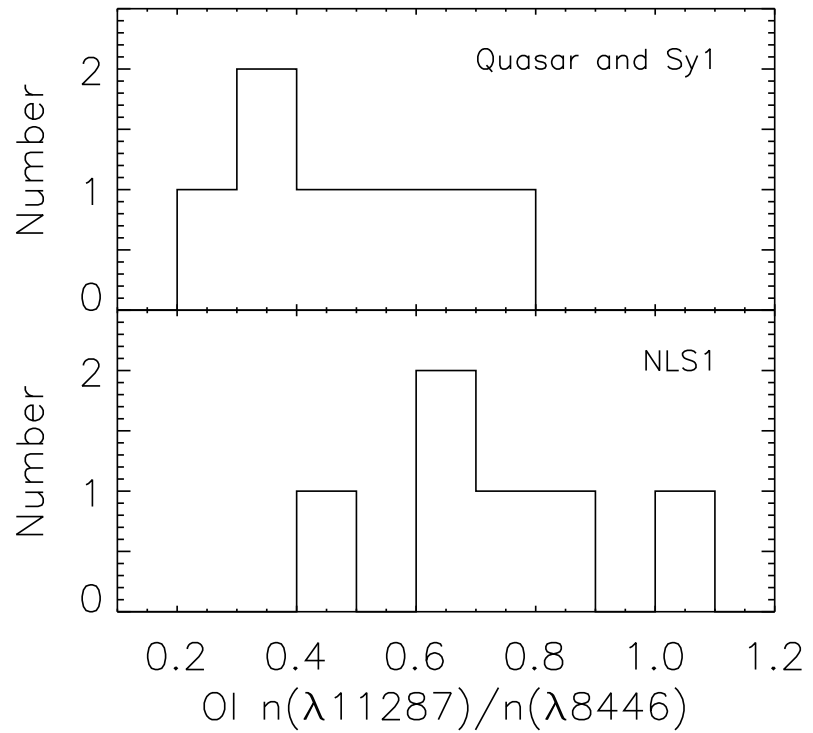


Fig. 11.— Number distributions of the O I $n(\lambda 11287)/n(\lambda 8446)$ ratios observed in AGNs. The top panel shows the distribution for quasars and Sy1, while the bottom panel shows the same for NLS1s.

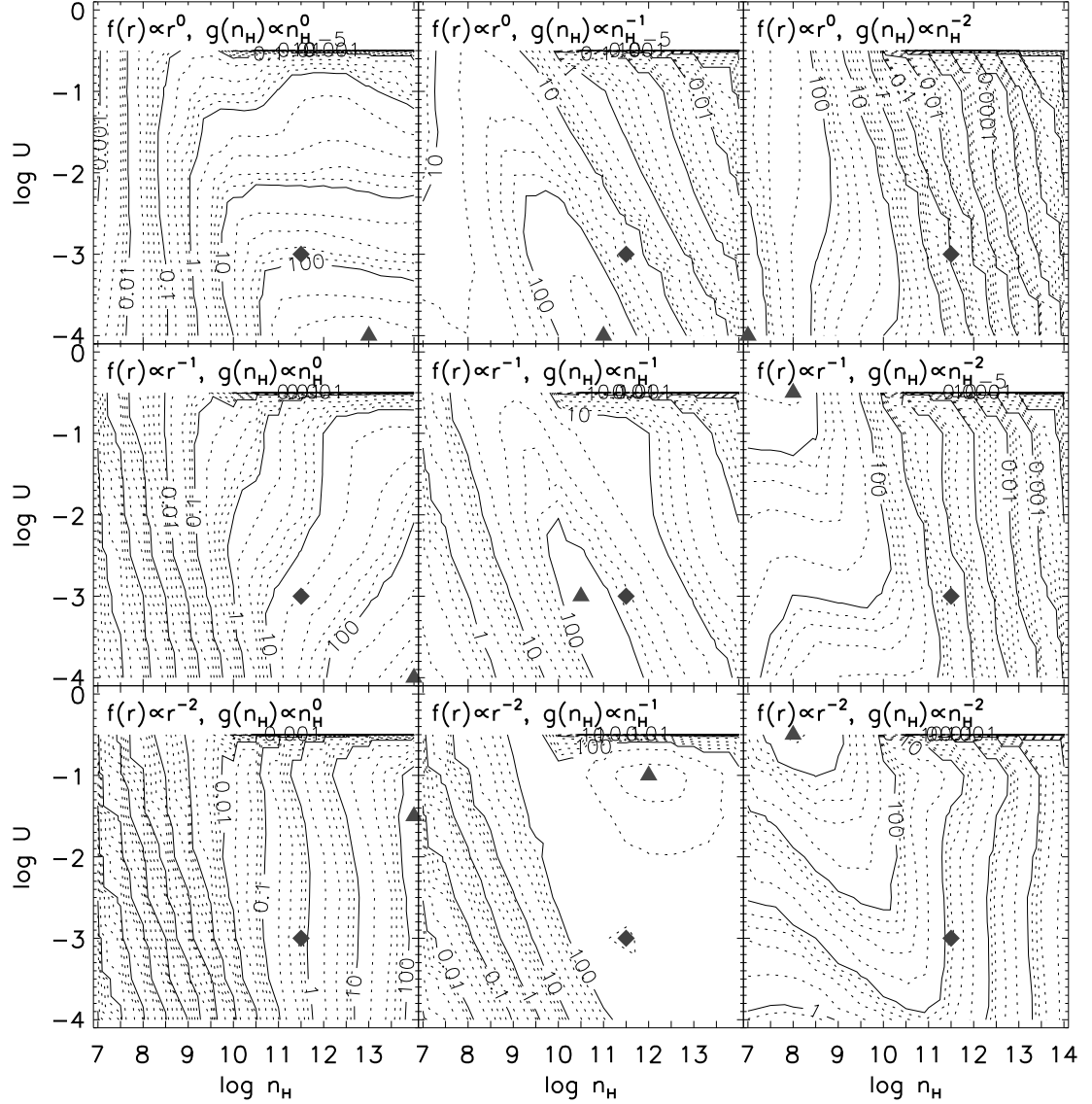


Fig. 12.— Distributions of the DF (see text for its definition) values for O I $\lambda 8446$ as a function of the gas density n_H and the ionization parameter U calculated in the standard model. Assumed distribution functions of the gas covering fraction and density are indicated at the top of each panel. Diamonds represent the best-fit parameters to the O I and Ca II observation, while triangles represent the parameters predicting the DF maxima.

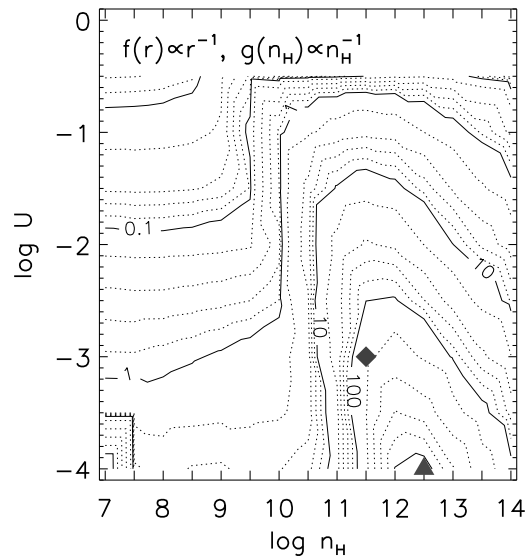


Fig. 13.— Distribution of the DF (see text for its definition) values for Ca II as a function of the gas density n_H and the ionization parameter U calculated in the standard model. Assumed distribution functions of the gas covering fraction and density are $f(r) \propto r^{-1}$ and $g(n_H) \propto n_H^{-1}$. A diamond represents the best-fit parameters to the O I and Ca II observation, while a triangle represents the parameters predicting the DF maximum.